

ALMA MATER STUDIORUM · UNIVERSITÀ DI BOLOGNA

---

Scuola di Scienze  
Dipartimento di Fisica e Astronomia  
Corso di Laurea Magistrale in Fisica del Sistema Terra

# Submesoscale Features in Regions with Different Baroclinic Deformation Radius

Relatore:  
Dott. Francesco Trotta

Presentata da:  
Francesco Maria Benfenati

Correlatore:  
Prof.ssa Nadia Pinardi

Anno Accademico 2021/2022



- *Working and playing are the very same thing* -  
(Scout "master word")

A mia moglie Chiara

I would like to thank Francesco Trotta who helped me carrying out this thesis work with great patience and kindness. Thank you to Nadia Pinardi, too, for allowing me to get in touch with her research group. Working together has been a great and inspiring experience to me, feeling at home.

## Abstract

*Ocean circulation occurs over a wide range of scales, from the planetary one of  $O(1000\text{ km})$  related to Ocean General Circulation (OGC), to the microscale ranging from less than a kilometer up to the millimeters. Kinetic energy is continuously transferred from large scales to small ones where it is dissipated as heat, passing through mesoscale eddies and submesoscale flows. Resolving the latter ones in ocean numerical simulations requires very fine resolution grids of  $O(1\text{ km})$ . This leads to great computational effort if submesoscale motion is solved directly by an OGC Model (OGCM). In this context, dynamical downscaling may be a useful approach for the purpose. It consists in generating high-resolution nested ("child") models based on large-scale information from an OGCM ("parent"), keeping reasonable computational cost.*

*In this study, a nested high-resolution model at  $1/48^\circ$  resolution is obtained through the NEMO-based SURF platform (Structured and Unstructured grid Relocatable ocean platform for Forecasting), from downscaling daily average fields of the large-scale CMEMS global model at  $1/12^\circ$  resolution. This allows to observe submesoscale features in two regions of the Northern Atlantic Ocean. While one region encompasses the Azores islands, going from  $35^\circ\text{N}$ ,  $23.5^\circ\text{W}$  to  $45^\circ\text{N}$ ,  $33.5^\circ\text{W}$ , the other one includes the Bermuda region, within the Gulf Stream, going from  $25^\circ\text{N}$ ,  $62^\circ\text{W}$  to  $35^\circ\text{N}$ ,  $72^\circ\text{W}$ . The simulation period goes from Jan, 4<sup>th</sup> to Jan, 12<sup>th</sup>, as submesoscale activity is considered more significant during winter months.*

*This thesis aims to conduct a preliminary analysis of the relation between baroclinic deformation radius and the onset of submesoscale activity, in the regions of interest. In fact, the two regions are distinguished by different values of the deformation radius, being characterized by different latitudes. For this purpose, many comparisons are made between parent and child resulting fields. In particular, the focus is on Mixed Layer Instability (MLI) studied through variables as Mixed Layer Depth (MLD), relative vorticity, horizontal and vertical velocities, Kinetic Energy (KE) and Brunt-Väisälä frequency.*

*From a mesoscale analysis based on parent model information, it appears in both regions restratification processes occur during the simulation days, along with MLD fluctuations of order  $O(\text{days})$ , typical of submesoscales. While parent model fails, the child one is able to detect MLI in both regions, better reproducing submesoscale horizontal and vertical currents. Furthermore,*

*from child high-resolution vorticity and temperature fields the presence of filaments and topographic wakes is assessed. Indeed, child model predicts higher KE in the surface layer, coherently with potential-to-kinetic energy conversion typical of MLI and frontogenesis. This provides a connection between mesoscale features and submesoscale currents generation: while in the Azores region MLI appears to play a key role in restratifying the water column, it does not seem the same in the Bermuda one where MLD oscillation is quite small. At lower latitudes, the deformation radius is larger and mesoscale eddies wider, affecting the vertical stratification more and longer. Thus, restratification processes would seem to be related to mesoscales rather than submesoscales. Here, MLI would still play a role in generating submesoscale currents, rather than restratifying, among other processes such as frontogenesis and topographic wakes.*

*In conclusion, the baroclinic deformation radius value does not seem to affect submesoscale processes activation, whereas it would seem to determine the importance of MLI in the restratification process. Comparing results from the two regions, it would seem the parent global model ability to detect submesoscale horizontal currents slightly increases at higher latitudes where the deformation radius is smaller. In this sense, benefits of a dynamical downscaling approach would seem more appreciable at lower latitudes.*

**keywords:**

Submesoscale, baroclinic deformation radius, Azores, Bermuda, Gulf Stream, high-resolution models, Structured and Unstructured grid Relocatable ocean platform for Forecasting (SURF), Mixed-Layer Instability.

# Abstract

- ITALIAN VERSION -

*La circolazione oceanica avviene su un'ampia gamma di scale, da quella planetaria di  $O(1000\text{ km})$  relativa alla circolazione generale dell'oceano, alla microscala che va da meno di un chilometro fino ai millimetri. L'energia cinetica è continuamente trasferita dalle scale grandi a quelle piccole dove viene dissipata sotto forma di calore, passando attraverso perturbazioni di mesoscala e flussi di sottomesoscala. Risolvere questi ultimi nelle simulazioni numeriche dell'oceano richiede griglie di risoluzione molto fini di  $O(1\text{ km})$ . Ciò porta a un grande sforzo computazionale se il moto alla sottomesoscala viene risolto direttamente da un modello di circolazione generale. In questo contesto, il cosiddetto "downscaling" (o ridimensionamento) dinamico può essere un utile approccio allo scopo. Esso consiste nel generare modelli nidificati ad alta risoluzione (chiamati figlio, "child") basati su informazioni a larga scala da un modello di circolazione generale (chiamato genitore, "parent"), mantenendo un costo computazionale ragionevole.*

*In questo studio, un modello nidificato ad alta risoluzione ( $1/48^\circ$ ) è ottenuto attraverso la piattaforma SURF ("Structured and Unstructured grid Relocatable ocean platform for Forecasting"), basata sul modello NEMO. Il modello nidificato è ottenuto tramite "downscaling" dei campi medi giornalieri dal modello globale CMEMS su larga scala (risoluzione di  $1/12^\circ$ ). Questo permette di osservare le caratteristiche della sottomesoscala in due regioni dell'oceano Atlantico settentrionale. Mentre una regione comprende le isole Azzorre e va da  $35^\circ\text{N}$ ,  $23.5^\circ\text{W}$  a  $45^\circ\text{N}$ ,  $33.5^\circ\text{W}$ , l'altra include la regione delle Bermuda, all'interno della Corrente del Golfo, e va da  $25^\circ\text{N}$ ,  $62^\circ\text{W}$  a  $35^\circ\text{N}$ ,  $72^\circ\text{W}$ . Il periodo di simulazione copre dal 4 al 12 gennaio 2021, poiché l'attività di sottomesoscala è ritenuta più intensa durante i mesi invernali.*

*Questa tesi si propone di condurre un'analisi preliminare della relazione fra il raggio di deformazione baroclinico e l'esordio dell'attività di sottomesoscala, nelle regioni di interesse. Infatti, le due regioni sono distinguibili per il valore raggio di deformazione, essendo caratterizzate da diverse latitudini. A questo scopo, vengono effettuati molti confronti fra i campi risultanti dal "parent" e dal "child". In particolare, ci concentriamo sull'instabilità dello strato mescolato (Mixed-Layer Instability, MLI) studiata attraverso variabili come la profondità dello strato mescolato (Mixed-Layer Depth, MLD), la vorticità*

relativa, le velocità orizzontali e verticali, l'energia cinetica e la frequenza di Brunt-Väisälä.

Da un'analisi della mesoscala basata sulle informazioni del modello "parent", risulta che in entrambe le regioni avvengono dei processi di ristrutturazione durante i giorni di simulazione, insieme a fluttuazioni del MLD di ordine  $O(\text{giorno})$ , tipiche della sottomesoscala. Mentre il modello "parent" risulta inadeguato, quello "child" è in grado di rilevare la MLI in entrambe le regioni, riproducendo meglio le correnti orizzontali e verticali alla sottomesoscala. Inoltre, dai campi di vorticità e temperatura ad alta risoluzione del "child" viene valutata la presenza di filamenti e scie topografiche. In effetti, il modello "child" prevede una maggiore energia cinetica nello strato superficiale, coerentemente con la conversione dell'energia potenziale in energia cinetica tipica della MLI e della frontogenesi. Ciò fornisce una connessione tra caratteristiche di mesoscala e la generazione di correnti alla sottomesoscala: mentre nelle Azzorre la MLI sembra svolgere un ruolo chiave nella ristrutturazione della colonna d'acqua, lo stesso non sembra nelle Bermuda dove l'oscillazione del MLD è abbastanza piccola. Alle latitudini inferiori, il raggio di deformazione è maggiore e i vortici di mesoscala più ampi, influenzando sulla stratificazione verticale di più e più a lungo. Pertanto, i processi di ristrutturazione sembrerebbero correlati alle mesoscale piuttosto che alle sottomesoscale. Qui, la MLI giocherebbe comunque un ruolo nella generazione di correnti alla sottomesoscala, piuttosto che ristrutturare, insieme ad altri processi come la frontogenesi e le scie topografiche.

In conclusione, il valore del raggio di deformazione baroclinico non sembra influenzare l'attivazione dei processi di sottomesoscala, mentre sembrerebbe determinare l'importanza della MLI nel processo di ristrutturazione. Confrontando i risultati nelle due regioni, sembrerebbe che la capacità del modello "parent" globale di rilevare correnti orizzontali alla sottomesoscala aumenti leggermente alle latitudini più elevate dove il raggio di deformazione è più piccolo. In questo senso, i vantaggi di un approccio di "downscaling" dinamico sembrerebbero più apprezzabili alle latitudini più basse.

**parole chiave:**

Sottomesoscala, raggio di deformazione baroclinico, Azzorre, Bermuda, Corrente del Golfo, modelli ad alta risoluzione, "Structured and Unstructured grid Relocatable ocean platform for Forecasting" (SURF), Mixed-Layer Instability.



# Contents

<b>1</b>	<b>Introduction</b>	<b>12</b>
1.1	Mesoscale Dynamics . . . . .	13
1.2	Submesoscale Dynamics . . . . .	15
1.2.1	Perspective on Submesoscale Currents . . . . .	15
1.2.2	Advantages of a High-Resolution Model Approach . . . . .	20
1.3	Baroclinic Deformation Radius and Modes of Motion . . . . .	24
1.4	Thesis Objectives . . . . .	29
<b>2</b>	<b>Model and Data</b>	<b>30</b>
2.1	Numerical Model . . . . .	31
2.1.1	NEMO-OCE . . . . .	31
2.1.2	SURF Platform . . . . .	34
2.2	Regions of Interest . . . . .	37
2.2.1	The Azores Region . . . . .	38
2.2.2	The Bermuda Region . . . . .	38
2.3	Experimental Setup . . . . .	38
2.3.1	Initial and Boundary Conditions . . . . .	39
2.3.2	Atmospheric Forcing . . . . .	39
2.3.3	Bathymetry and Coastlines . . . . .	39
2.3.4	Tides . . . . .	41
2.3.5	Model Set-Up . . . . .	41
<b>3</b>	<b>Mesoscale Analysis in the Azores and Bermuda Regions</b>	<b>44</b>
3.1	Horizontal Features . . . . .	45
3.2	Vertical Insight . . . . .	49

<b>4</b>	<b>Submesoscale Analysis in the Azores and Bermuda Regions</b>	<b>55</b>
4.1	Parent-Child Comparison . . . . .	56
4.1.1	Horizontal Features . . . . .	56
4.1.2	Vertical Insight and Mixed-Layer Instability . . . . .	65
4.2	Submesoscale Structures from High-Resolution Fields . . . . .	76
<b>5</b>	<b>Conclusion</b>	<b>79</b>
	<b>Bibliography</b>	<b>81</b>

# Chapter 1

## Introduction

### Contents

---

<b>1.1 Mesoscale Dynamics</b> . . . . .	<b>13</b>
<b>1.2 Submesoscale Dynamics</b> . . . . .	<b>15</b>
1.2.1 Perspective on Submesoscale Currents . . . . .	15
1.2.2 Advantages of a High-Resolution Model Approach	20
<b>1.3 Baroclinic Deformation Radius and Modes of Motion</b> . . . . .	<b>24</b>
<b>1.4 Thesis Objectives</b> . . . . .	<b>29</b>

---

Ocean circulation occurs over a wide range of scales, from the planetary one of  $O(1000km)$  related to Ocean General Circulation (OGC), to the microscale ranging from less than a kilometer up to the millimeters. Kinetic energy is continuously transferred from large scales to small ones where it is dissipated as heat, passing through mesoscale eddies and submesoscale flows. While mesoscale ( $O(100km)$ ) has been extensively investigated, during the last few years the less known realm of submesoscale dynamics ( $O(1km)$ ) has gained larger concern among oceanographers. Nevertheless, much work still needs to be done to a better understanding.

In the present thesis work, we employ a high-resolution downscaling approach for studying submesoscale features in two regions of the North At-

lantic ocean. The study is carried out during a short winter period (January 4<sup>th</sup>-12<sup>th</sup>, 2021) and the regions are chosen to be characterized by a different baroclinic deformation radius. Submesoscale features are analysed and compared to mesoscale ones and the benefits of a dynamical downscaling approach are pointed out.

In this chapter, we describe theoretical aspects and previous studies about mesoscale and submesoscale dynamics. Furthermore, we bring points in favor of a dynamical downscaling approach for studying the latter one. Lastly, we discuss the baroclinic Rossby radius of deformation, an important quantity when dealing with scale transition from meso to submesoscale.

## 1.1 Mesoscale Dynamics

All regions of the ocean have some level of *eddy variability* which is defined as *the departure of instantaneous velocities or sea surface/isopycnal heights from the mean* (Talley et al., 2011).

From a global ocean point of view, variability takes various shapes which are responsible for along-isopycnals stirring: from random noise to waves, up to closed, coherent structures. For example, warm- and cold-core rings generated by the meandering of major currents like the Gulf Stream (Fig. 1.1) are large, closed structures that one might typically associate with eddies. On the other hand, eddy variability in the central parts of the gyres may look more like spectral noise. Some kinds of eddies extend from the sea surface to the bottom, while others are concentrated in the surface layer

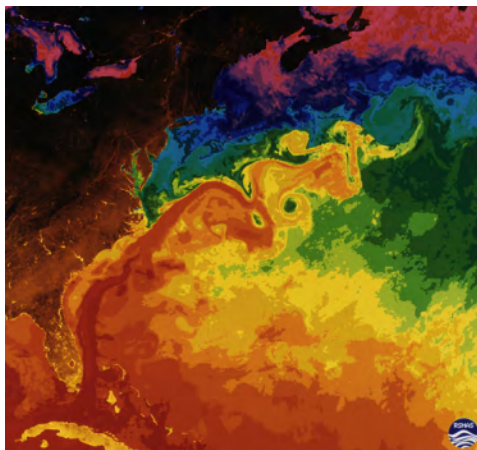


**FIGURE 1.1:** *Gulf Stream meanders and rings from sea surface temperature satellite measurements (Talley et al., 2011).*

or entirely embedded within sub-surface layers. Horizontal eddy length scales are typically of order  $O(10km)$  up to  $O(100km)$ . Timescales are typically

weeks to months. This is considered to be the ocean's *mesoscale*.

### General Aspects

Mesoscales are associated with planetary waves such as Rossby and Kelvin waves. The most important length scale for this variability is the Rossby deformation radius, which depends on latitude and vertical stratification. It will be discussed in Sec. 1.3. Oceanic mesoscale eddies are in geostrophic balance, i.e. balance between horizontal pressure gradient forces and Coriolis force. Furthermore, they contain the greatest fraction of kinetic energy in the ocean and play an important role in the transport of heat, carbon and other climatically important tracers across the oceans.

### Theoretical Justification

Mesoscale eddies justification is obtained perturbing the geostrophic equation of motion. Geostrophy is the balance between pressure and rotational effects, in this context referred to a planetary scale. It is described by the equation set

$$\begin{cases} f v_g = g \frac{\partial \eta}{\partial x} \\ f u_g = -g \frac{\partial \eta}{\partial y} \end{cases}, \quad (1.1)$$

where  $f, g$  are respectively the Coriolis parameter and the gravitational acceleration module;  $\vec{u}_g = (u_g, v_g)$  is the geostrophic (horizontal) velocity field;  $(x, y)$  are the horizontal coordinates and  $\eta$  is the free surface height. Through the *perturbation theory*, from Eq. 1.1 one obtains conservation of the *quasi-geostrophic vorticity*  $\Pi$ , as

$$\frac{D}{Dt} \Pi = 0 \quad \text{with } \Pi = [\xi_z + \beta y - \sigma(\eta_0, \eta_B)] \quad ; \quad (1.2)$$

where  $\xi_z$  and  $\beta y$  are respectively the vertical relative and planetary vorticity;  $\sigma$  is the term due to water column stretching which depends on the geostrophic free surface height ( $\eta_0$ ) and the bottom bathymetry ( $\eta_B$ ). Eq. 1.2 predicts mesoscale features such as the Rossby waves formation.

As it appears, mesoscale eddies are the manifestation of imbalances in the geostrophic field. Thus, they are the first important step in the energy cascade from planetary scale to microscale where it is dissipated.

### Rossby number

The Rossby number is a fundamental nondimensional quantity in Geo-

physical Fluid Dynamics (GFD), as it can be used for studying the various motion scales. It is defined as

$$R_o := \frac{\xi_z}{f} \equiv \frac{U}{fL} \quad , \quad (1.3)$$

where  $f$  is the Coriolis parameter and  $\xi_z$  the relative vorticity along depth direction. In a scale analysis, one may obtain  $\xi_z$  as  $U/L$ , where  $U$  is the horizontal velocity order of magnitude while  $L$  is the horizontal length scale. The Rossby number results from the ratio between inertial forces (momentum advection) and the Coriolis force. Thus, it expresses the importance of rotational effects in the context of a certain motion. The greater  $R_o$  gets, the less dominant Earth's rotation becomes, with the onset of restratification processes.

For a planetary flow, with  $L \approx O(1000km)$  and small  $U$ , we typically have  $R_o \ll 1$  which defines the qualification of "flow in geostrophic balance". The Rossby number increases with decreasing scales. At submesoscale regime, we typically have  $R_o > 1$ .

## 1.2 Submesoscale Dynamics

The submesoscales are emerging as an important dynamical regime due to their impacts on vertical motion in the upper ocean and for providing a dynamical connection to the even smaller scales where mixing and dissipation take place. They occur on an intermediate horizontal scale of order  $O(1km)$ , ranging from  $0.1km$  to  $10km$ , and time scales of hours to days. Vertical scale goes from  $0.01km$  to  $1km$ .

In the following subsections, we try to give a general picture about the state-of-the-art of submesoscale studies during the last years, based on the perspective article by [McWilliams \(2016\)](#) and following works. Attention will be given to submesoscale variability results obtained through high-resolution simulations.

### 1.2.1 Perspective on Submesoscale Currents

Submesoscale Currents (SMCs) spontaneously emerge from mesoscale eddies and boundary currents, especially in the neighborhood of the Surface and Bottom Boundary Layers (SBL and BBL). They are partly constrained by

geostrophic, hydrostatic momentum-balance, but also break this balance at smaller scales and exhibit a forward energy cascade to dissipation and diapycnal mixing (McWilliams, 2016). They result to be an important element in general circulation from several perspectives. Still, there is much to quantify about their contributions to oceanic system dynamics.

In the following paragraphs we refer to McWilliams (2016), even if not specified.

### Role in General Circulation

From an energy point of view, when the ocean currents are well separated from the bottom, significant eddy energy sinks in mesoscale motion may happen in the ocean interior and near the surface, instead of in the BBL. This reveals where SMCs are a major conduit to dissipation, breaking the balance constraint and exhibiting a forward energy cascade. For example, in Ocean General Circulation Models (OGCMs), even with mesoscale-resolving grids there is a significant energy sink away from the bottom that reveal local submesoscale forward cascade processes.

SMC dynamics has an important role, too, in numerical forecasts initialization through measurements. This requires a momentum balance constraint for removing inertia-gravity waves which would make the scheme diverging. Indeed, implementation of balanced initialization schemes have often failed to converge due to the presence of SMC dynamics.

In the context of thermohaline circulation, SMCs may be a contributing factor. In fact, this circulation can only occur if the diapycnal material eddy diffusivity is large enough to allow dense water transformation to lighter one. In this sense, a significant forward energy cascade by SMCs may also contribute appreciably to enlarge the diffusivity value. This seems especially plausible near the surface and bottom, but it is a serious possibility in the interior, too.

SMCs have a large vertical velocity, especially within the SBL, which is much larger than for mesoscale eddies and with larger space and time scales than for Boundary Layer (BL) turbulence. This leads to large material eddy fluxes. In particular, SMCs manifest both *frontogenesis* and *Mixed-Layer Instability* (MLI), i.e. baroclinic instability of a weakly stratified layer in presence of a horizontal buoyancy gradient. Thus, submesoscale processes contribute to adiabatic restratification that opposes the diabatic mixing by

BL turbulence. A conversion of potential to kinetic energy occurs, revealing frontogenesis and MLI as two of the possible mechanisms for SMCs generation.

### Submesoscale Coherent Vortices

The Submesoscale Coherent Vortices (SCVs) are probably the earliest known class of SMCs. They can be detected as *spatially sparse but abundant instances of an extreme chemical anomaly in hydrographic profiles, in association with a local interior minimum in vertical stratification* (McWilliams, 2016). SCVs result to be gradient-wind balanced anticyclonic vortices that trap their core water materials and live long enough, sometimes up to years, to be advected far away from their generation site. This seems the only submesoscale process overcoming the time scale of days. Thus, SCVs have a long-range transport capacity for dissolved materials. From measurements, it appears that SCVs are common throughout the interior of the ocean. Comparing their distinctive concentration suites to the persistent chemical geography in the ocean, one may indicate their origin locations. The dominance of anticyclonic SCVs over cyclonic ones is still a controversial issue. It was originally interpreted as due to local diapycnal mixing events that create a stratification anomaly, followed by gradient-wind adjustment of the vortical flow. A more refined interpretation is that SCVs usually form from separating, violently unstable boundary currents that induce strong mixing and roll up into vortices.

### Generation Mechanisms

SMCs are generated through mechanisms such as instabilities, frontogenesis and topographic wakes. Here, we focus on the SBL and BBL as the primary generation sites, but interior generation is also a viable process.

1. MIXED-LAYER INSTABILITY. Baroclinic instability is a first direct cause of SMCs generation in the surface layer.

Baroclinic instability centered in the pycnocline is understood to be a primary generating process for mesoscale currents. There, stratification is stronger and mesoscale currents are generated with horizontal scales around the baroclinic deformation radius  $l_d$ . In the same way, baroclinic instability generates SMCs in the surface layer. Here, stratification is weaker due to turbulent mixing. However, one may still

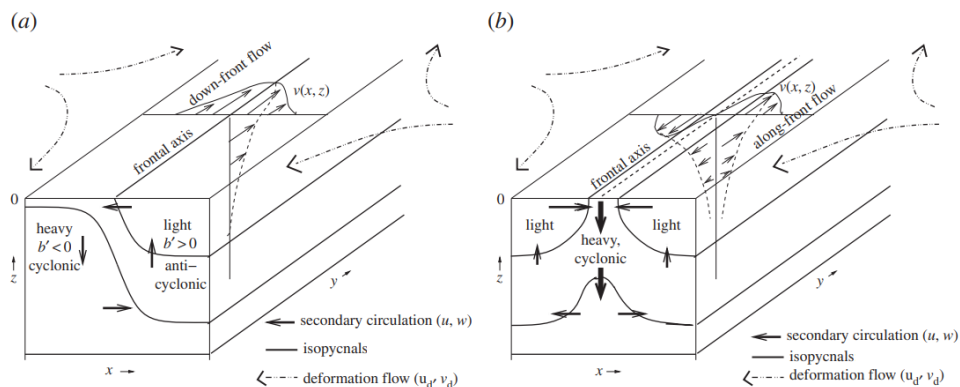


**FIGURE 1.2:** Schematics of frontogenesis processes generating submesoscale features as fronts (a) and filaments (b), by [McWilliams \(2016\)](#).

define the deformation radius for a weakly stratified surface layer

$$l_s = \frac{N_s h_b}{f_0}, \quad (1.4)$$

where  $N_s \approx 10^{-3} \text{s}^{-1}$  is the Brunt-Vaisala frequency,  $h_b \approx 10^2 \text{m}$  is the surface layer thickness and  $f_0 \approx 10^{-4} \text{s}^{-1}$  the Coriolis parameter. Thus, we obtain  $l_s \approx 1 \text{ km}$  ( $\ll l_d$ ) which is the horizontal length scale of SMCs, pointing out that MLI generates fluctuations within the submesoscale range.

Ocean satellite images show an abundance of sea-surface temperature gradients, and the surface layer is often nearly-neutrally stratified. Hence, the conditions for MLI (and SMCs generation) are commonly satisfied.

Sometimes, the submesoscale eddy field develops sharp frontal features (i.e. strong gradients) that have an along-front size close to the eddy scale. In this regime, the phenomenon is also called Mixed-Layer Eddies (MLEs). Their frontal structures are an indication of the finite Rossby number values typical of SMCs, as well as manifestation of frontogenesis within the eddies.

2. STRAIN-INDUCED FRONTOGENESIS. *Fronts* and *filaments* are typical submesoscale features in oceanic surface fields such as vertical vorticity, sea-surface temperature or material concentration. These distinguishable patterns are in form of sharp edges (fronts) or line patterns

(filaments), usually related to marked buoyancy gradients. They are formed through a process called *frontogenesis* which is an extremely efficient way to transfer variance and energy density to smaller scales. During surface-layer frontogenesis caused by a large-scale deformation flow, an ageostrophic secondary circulation is established (Fig. 1.2). For fronts, we might draw the process as two water masses encountering, each with different density. Due to gravity, an overturning cell is formed, with upwelling and surface divergence on the lighter side, while downwelling and surface convergence on the dense side. Furthermore, a partially geostrophic downfront flow occurs, due to rotational effects. As regards filaments, the process is quite the same but we have a water mass embedded in a lighter one. In this case, two overturning cells and along-side flows (in both directions) are established. The two secondary circulation cells come together in a central downwelling branch underneath a surface convergence line. Both processes have their energy source in the background available potential energy, which is in the surface layer, and both are characterized by a restratification buoyancy flux.

Frontogenesis and MLI work in pair for generating SMCs. In fact, MLI provides a potential energy source which can be converted to kinetic one, while frontogenesis characterizes the system advective evolution towards frontal and filamentary lines.

3. TURBULENT THERMAL WIND. Both mechanisms seen so far are formulated within a conservative flow paradigm. Nevertheless, the oceanic surface layer is almost always turbulent, hence non-conservative. What does seem common in fronts and filaments, is an approximate linear momentum-balance called Turbulent Thermal Wind (TTW), plus an incompressible mass balance. TTW is simply a composite generalization of geostrophic, hydrostatic balance, on one hand, and Ekman boundary-layer balance on the other. This further implies that frontogenesis can occur because of TTW, in association with the surface convergence lines on the dense side of a front and in the centre of a filament. This process does not replace but completes the two seen so far. Of course, these generation and maintenance processes occur in parallel with all the destruction ones for fronts and filaments. We are talking about frontal arrest, fragmentation by frontal instability

and vortex formation, weakening by SBL turbulent diffusion, or others contributing to forward energy cascade.

4. TOPOGRAPHIC WAKES. Submesoscale motions can arise from the interaction between the oceanic flow and the topography, which generates wakes. This is a quite common framework in fluid dynamics (e.g. horizontal flow past a vertical cylinder), when the Reynolds number is large enough. Respect to the well-known von Karman vortex street, here several important dynamical differences should be noticed. Firstly, rotation and stratification are significant. Secondly, the wakes and their evolution are more fully three-dimensional due to non-uniformity along depth of both the incoming flows and the boundary shape. Lastly, except for coastal cliffs, the obstacle is essentially only a bottom, not a side. This means that the vorticity-generating site is the BBL.

### 1.2.2 Advantages of a High-Resolution Model Approach

Being the SMCs strongly related to the onset of turbulence, their dynamics is advective, hence nonlinear and complex to be treated theoretically. Still, they are difficult to be detected since the scale at which they occur,  $O(1km)$ , is small for satellite observation but large for shipboard instrument detection. Furthermore, they are often difficult to distinguish from inertia-gravity waves in single-point time series or individual vertical profiles (McWilliams, 2016). Despite few attempts of investigating them through satellite data (Essink et al., 2019) or drifters (Chapron et al., 2020), a privileged way of studying SMCs seems to be through numerical simulations as computational oceanography is carving out its space among the marine sciences (Haine et al., 2021).

Resolving submesoscale dynamics in ocean numerical simulations requires very fine resolution grids of  $O(1\text{ km})$ . This leads to extreme computational effort if submesoscale motion is solved directly by an Ocean General Circulation Model (OGCM). On the other hand, the increasing computer power is making possible to run very High-Resolution (HR) models in restrained domains, able to detect submesoscale activity. In this context, dynamical downscaling may be a useful approach for the purpose. It consists in generating local HR nested models based on large-scale information from OGCMs, keeping reasonable computational cost. The nested HR simulation is called

"child", starting from the nesting coarser model called "parent". Multiple nestings may also be exploited for reaching greater accuracy.

The employ of HR models in oceanography is really an impending issue. It has drastically increased the size of model outputs, making it difficult to transfer and analyze the data. Nonetheless, it is of primary importance to assess more systematically the realism of these models, to reap the maximum benefits. Just recently, [Uchida et al. \(2022\)](#) have proposed a cloud-based analysis framework in the context of Pangeo Project, which aims to tackle such challenges.

### **SURF Downscaling Approach**

Among nesting and downscaling procedures, the NEMO-based "Structured and Unstructured grid Relocatable ocean platform for Forecasting" called SURF has been recently developed within Bologna University ([Trotta et al., 2016](#)). This modelling framework has turned out to be beneficial for studying submesoscale activity in the Gulf of Taranto, Italy ([Trotta et al., 2017](#)). Furthermore, it has proved useful for investigating coastal and near coastal areas and issues related to disaster risk reduction. In fact, the benefits of SURF downscaling approach result to be the supply of more detailed information to search and rescue operations, along with improvements in forecasting storm surges, currents in narrow straits and oil spill trajectories ([Trotta et al., 2021](#)).

### **Submesoscale Variability and Seasonality**

Similarly to the SURF case, during the last years, such kind of submesoscale-permitting High-Resolution (HR) simulations have also been employed with success for investigating submesoscale variability and seasonality among the global ocean.

As concerns the Northern Atlantic ocean, [Mensa et al. \(2013\)](#) have studied submesoscale dynamics seasonality in the Gulf Stream region, while [Ajayi et al. \(2020\)](#) have analyzed spatial and temporal variability in the North Atlantic eddy field, considering a wider region. The high-resolution approach allowed both authors to find interesting common results: (i) the strong seasonality shown by submesoscale eddies, with stronger features mostly present during winter; (ii) the link between submesoscale activity and mixed layer instability.

In the Kuroshio region, [Rocha et al. \(2016\)](#) have studied submesoscale seasonality. They provided model-based evidence that the vigorous seasonal cycle of the mixed layer modulates upper-ocean submesoscale turbulence. Summertime restratification weakens submesoscale turbulence but enhances inertia-gravity waves near the surface. Thus, they found out that submesoscale turbulence and inertia-gravity waves undergo vigorous out-of-phase seasonal cycles in this region.

Lastly, [Sasaki et al. \(2020\)](#) employed a submesoscale-permitting hindcast simulation, from 1990 to 2016, for investigating interannual to decadal variations of submesoscale motions in the Pacific. The study was carried out in the subtropical Northwestern Pacific including the subtropical counter-current. They found submesoscale Kinetic Energy (KE) is characterized by strong interannual and decadal variability. They suggested submesoscale motions might explain the impact on decadal mesoscale KE variability associated with the Pacific decadal oscillation phenomenon.

### **Other Results from High-Resolution Simulations**

The High-Resolution (HR) approach really seems to be a successful strategy for studying various aspects of submesoscale, including its variability among the global ocean. Our work aims to be included in this research framework. However, literature regarding submesoscale spatial variability is poor as it is still a frontier issue. During the last years, few researches have investigated the topic among the global ocean. Nevertheless, the number of individual HR simulations carried out in single ocean areas has increased, making submesoscale features and processes clearer. Here, we try to collect recent results obtained through HR simulations in few ocean regions, as it may be a starting point for dealing with spatial variability. In particular, it may be useful to assess our results. We focus on the *Kuroshio* and *Gulf Stream* regions, where submesoscale processes are favoured due to the presence of boundary currents.

- KUROSHIO REGION.

Using both satellite measurements and high-resolution simulations combined, [Zhang et al. \(2021\)](#) analyse submesoscale characteristics of a typical anticyclonic mesoscale eddy in the Kuroshio extension. They show that submesoscale Kinetic Energy (KE) is in close connection with KE of geostrophic velocity. Frontogenesis may be an important

way to enhance the submesoscale kinetic energy in the eddy periphery. Furthermore, they find submesoscale processes can induce strong vertical velocity which can reach a depth of hundreds of meters. They conclude that submesoscale processes can provide an efficient way for sea surface-internal material exchanging and air-sea interactions.

[Cao et al. \(2021\)](#) investigate the submesoscale energy budget in the upper ocean of the Kuroshio extension, based on a series of nested numerical simulations. They find that the submesoscale Kinetic and potential Energy are mainly contained in the mixed layer and energized through both barotropic (shear production) and baroclinic (buoyancy production) routes. However, baroclinic instability seems to be more efficient in transferring energy. Furthermore, a transition from inverse to forward KE cascade occurs.

Lastly, [Cheng et al. \(2020\)](#) study the submesoscale features coming out from interaction between the strong Kuroshio current and the southernmost tip of Taiwan. They observe a recirculation flow induced in the immediate lee of the cape as a result of flow separation. From the recirculation that occurs, eddies are shed, corotate and merge further downstream. Their shedding period is strongly modulated by either diurnal or semidiurnal tidal flows.

- GULF STREAM REGION.

In this region, [Gula et al. \(2016\)](#) study a frontal eddy near the southeastern U.S. seaboard, propagating between the Charleston Bump and Cape Hatteras. Through a very high-resolution simulation, they find a richness of submesoscale structures inside the frontal eddy, which reveal to be cyclonic vortices. Upwelling in the cold core of the eddy is intensified as the resolution is increased. In particular, submesoscale patterns create localized regions of intense upwelling bringing additional cold and freshwater. Thus, the emerging submesoscale features could potentially impact the biological production in the area. Lastly, the frontal eddy locally creates a strong southward flow against the shelf. This leads to topographic generation of submesoscale centrifugal instability and mixing.

In the same area, [Gula et al. \(2019\)](#) employ a submesoscale-resolving realistic simulation to reproduce SCVs observed through seismic images and glider sections. Analysing their generation mechanism, it

results SCVs are primarily generated where the Gulf Stream meets the Charleston Bump, a deep topographic feature, due to the frictional effects and intense mixing in the wake of the topography. These kind of submesoscale structures can transport waters from the Charleston Bump's thick bottom mixed layer over long distances and spread them within the subtropical gyre.

In the nearby of the Gulf Stream, that is in the Gulf of Mexico, [Liu et al. \(2021\)](#) investigate submesoscale processes importance in mixing across the mixed layer. This is done analyzing the trajectories of Lagrangian particles released multiple times at the ocean surface and below the mixed layer, both in mesoscale and submesoscale permitting simulations. They point out that submesoscale circulations are responsible for greater vertical transport across fixed depth ranges and across the mixed layer, too, both into it and away from it. This seems to be true in all seasons, but more significant during winter. Furthermore, they find that in a large mesoscale eddy, upwelling into the mixed layer is the major contributor to the vertical fluxes, despite its clockwise circulation. Indeed, this is opposite to the behavior simulated in the mesoscale resolving case, showing once again the hints resulting from a HR approach.

### 1.3 Baroclinic Deformation Radius and Modes of Motion

Rossby radius of deformation is an important quantity related to mesoscale processes, useful to investigate transition from mesoscale to submesoscale. It is defined as the *distance over which the gravitational tendency to render the free surface flat is balanced by the tendency of the Coriolis acceleration to deform the surface* ([Pedlosky, 1987](#)). If we consider a barotropic ocean model, the corresponding Rossby radius is called *barotropic*, while for a stratified ocean model it is called *baroclinic*. In the last case, various deformation radii exists, as many as the number of allowed baroclinic modes of motion. The analysis of the local *dynamic baroclinic modes of motion* and their respective *baroclinic deformation radii* is a useful way for studying the complex issue of ocean vertical stratification. For our purpose, the deformation radius is a helpful quantity for understanding the horizontal scale below which

restratification effects activate through submesoscale processes.

### Theoretical Framework

For deriving the *baroclinic deformation radius* and the *modes of motion*, we start from the nondimensional linearized QuasiGeostrophic (QG) equation of motion (Grilli et al., 1999). It describes the motion of the field geostrophic component resulting from the balance between pressure and Coriolis forces:

$$\frac{\partial}{\partial t} \left[ \frac{\partial^2 p_0}{\partial x^2} + \frac{\partial^2 p_0}{\partial y^2} + \frac{\partial}{\partial z} \left( \frac{1}{S} \frac{\partial p_0}{\partial z} \right) \right] + \beta \frac{\partial p_0}{\partial x} = 0 \quad , \quad (1.5)$$

with Boundary Conditions

$$\frac{\partial}{\partial t} \left( \frac{\partial p_0}{\partial z} \right) = 0 \text{ at } z = 0, 1 \quad ; \quad (1.6)$$

where  $p_0$  is the pressure term expanded at the first order of the Rossby number  $\epsilon$ , while  $\beta$  is the *beta Rossby number*.  $S$  is the stratification parameter, defined as

$$S(z) = \frac{N^2(z)H^2}{f_0^2 L^2} \quad , \quad (1.7)$$

with the Brunt-Vaisala frequency  $N$  obtained as

$$N = \left[ -\frac{g}{\rho_0} \frac{\partial \rho_s}{\partial z} \right]^{\frac{1}{2}} \quad (\rho_s \text{ basic mean stratification}), \quad (1.8)$$

where  $\rho_0 = 1025 \text{ kg/m}^3$  is the reference density value. Here,  $L$  and  $H$  are respectively the horizontal and vertical scales of motion, through which the QG equation is made nondimensional. We assume  $L \approx O(100 \text{ km})$ , corresponding to mesoscale, and  $H \approx O(1 \text{ km})$ , equal to the mean depth of the considered region. The *Coriolis parameter* is assumed  $f_0 = 10^{-4} \text{ 1/s}$  while the gravitational acceleration is  $g = 9.806 \text{ m/s}^2$ .

If we consider a solution to the QG equation of type

$$p_0(x, y, z, t) = f(x, y, t) \Phi(z) \quad \left( f = \Re \left[ e^{i(kx + ly - \sigma t)} \right] \right) \quad (1.9)$$

where  $\Phi(z)$  is the vertical structure function, it follows

$$\frac{\partial}{\partial t} \left[ \frac{\partial^2 f}{\partial x^2} + \frac{\partial^2 f}{\partial y^2} - \lambda \right] + \beta \frac{\partial f}{\partial x} = 0 \quad ; \quad \lambda = - \left[ \frac{\beta k}{\sigma} + k^2 + l^2 \right] \quad . \quad (1.10)$$

### 1.3. Baroclinic Deformation Radius and Modes of Motion

---

This necessary leads to the eigenvalues/eigenvectors equation

$$\boxed{\frac{d}{dz} \left( \frac{1}{S} \frac{d\Phi_n}{dz} \right) = -\lambda_n \Phi_n \quad \left( B.C. \quad \frac{d\Phi_n}{dz} \Big|_{z=0}^{z=1} = 0 \right)} \quad (1.11)$$

where the eigenvectors  $\Phi_n$  are the vertical structure functions, each corresponding to a mode of motion  $n = 0, 1, 2, \dots$ , while the eigenvalues  $\lambda_n$  may be used for computing the *baroclinic Rossby deformation radius*

$$R_n = \frac{1}{\sqrt{\lambda_n}} \quad (1.12)$$

for each mode  $n$ . As shown in [Grilli et al. \(1999\)](#), eigenvalues are null or positive. The trivial eigenvalue  $\lambda = 0$  corresponds to the barotropic mode  $\Phi_0(z) = 1$ , while  $\lambda = 1, 2, \dots$  correspond to the baroclinic modes  $\Phi_{1,2,\dots}(z)$ .

#### Analytical Solutions

The above eigenvalues/eigenvectors Eq. 1.11 is difficult to solve analytically, except for particular shapes of the Brunt-Vaisala (BV) frequency profile  $N(z)$ . In fact, for a constant profile  $N(z) = N_0 = const$ , the solution is well known ([Pedlosky, 1987](#)):

$$\Phi_n(z) = \cos(n\pi z) \quad , \quad \lambda_n = \frac{n^2 \pi^2}{S} \quad . \quad (1.13)$$

For exponential BV frequency profiles of type  $N(z) = N_0 e^{\alpha z}$ , [LaCasce \(2012\)](#) suggests a theoretical solution for the vertical structure function, of type

$$\Phi_n(z) = A e^{\alpha z/2} \left[ Y_0(2\gamma_n) J_1(2\gamma_n e^{\alpha z/2}) - J_0(2\gamma_n) Y_1(2\gamma_n e^{\alpha z/2}) \right] \quad (1.14)$$

where  $A$  is the oscillation amplitude,  $J_n$  and  $Y_n$  are Bessel functions of respectively the first and second kind, with  $n$  the function order. The eigenvalues  $\lambda_n$  are contained in

$$\gamma_n = \frac{N_0 \lambda_n}{\alpha f_0} \quad . \quad (1.15)$$

The eigenvalues may be found applying the bottom Boundary Condition (at  $z = 1$ ) to solution 1.14:

$$J_0(2\gamma_n) Y_0(2\gamma_n e^{\alpha/2}) - Y_0(2\gamma_n) J_0(2\gamma_n e^{\alpha/2}) = 0 \quad . \quad (1.16)$$

### Numerical Implementation

Apart from cases of constant or exponential stratification, numerical methods should be employed for resolving Eq. 1.11 in case of realistic BV frequency profiles. For our purpose, in this thesis we employ the deformation radius values computed by LaCasce et al. (2020) for the global ocean, which will be shown in Chap. 2. They are obtained through a more sophisticated procedure than the one we approach to describe. However, here we suggest a possible method which might be implemented for computing the deformation radius and the corresponding vertical structure functions, as it can still provide the reader with the idea behind it.

1. We carry out a change of variables (Grilli et al., 1999)

$$w = \frac{1}{S} \frac{d\Phi}{dz} \Rightarrow \Phi(z) = \int_0^z S w dz + \Phi_0 \quad \left( \Phi_0 = \Phi|_{z=0} = \text{const} \right) \quad (1.17)$$

so that

$$\frac{dw}{dz} = -\lambda \Phi = -\lambda \left( \int_0^z S w dz + \Phi_0 \right) \quad (1.18)$$

and problem 1.11 becomes

$$\boxed{\frac{d^2 w}{dz^2} = -\lambda S w} \quad \left( \text{B.C. } w = 0 \quad \text{at } z = 0, 1 \right) \quad , \quad (1.19)$$

obtaining a simple eigenvalues/eigenvectors problem of known resolution.

2. Parameter  $S$  is *linearly interpolated*, so that we can redefine the problem on an equally spaced vertical grid of step  $1m$  which becomes  $\Delta z = \frac{1m}{H}$  in the nondimensional problem.
3. The *finite difference matrix* corresponding to operator  $\frac{\partial^2}{\partial z^2}$  is computed employing fourth-order centered finite difference method  $O(\Delta z^4)$ . The 1D profile  $S$  is rearranged to occupy the diagonal of a square matrix.

### 1.3. Baroclinic Deformation Radius and Modes of Motion

---

Thus, problem 1.19 becomes

$$\begin{aligned}
 & \frac{1}{12\Delta z^2} \begin{bmatrix} 0 & 0 & 0 & 0 & 0 & 0 & \dots & 0 \\ 12 & -24 & 12 & 0 & \dots & 0 & \dots & 0 \\ -1 & 16 & -30 & 16 & -1 & 0 & \dots & 0 \\ 0 & -1 & 16 & -30 & 16 & \dots & \dots & 0 \\ \vdots & \ddots & \ddots & \ddots & \ddots & \dots & \dots & \vdots \\ 0 & \dots & \dots & 0 & 0 & 12 & -24 & 12 \\ 0 & \dots & 0 & 0 & 0 & 0 & 0 & 0 \end{bmatrix} \begin{bmatrix} w_0 \\ w_1 \\ w_2 \\ \vdots \\ \vdots \\ w_{N-1} \\ w_N \end{bmatrix} = \\
 & = -\lambda \begin{bmatrix} S_0 & 0 & 0 & 0 & \dots & \dots & 0 \\ 0 & S_1 & 0 & 0 & \dots & \dots & 0 \\ 0 & 0 & S_2 & 0 & \dots & \dots & 0 \\ 0 & 0 & 0 & S_3 & \dots & \dots & 0 \\ \vdots & \ddots & \ddots & \ddots & \ddots & \ddots & \vdots \\ 0 & \dots & \dots & \dots & 0 & S_{N-1} & 0 \\ 0 & \dots & \dots & \dots & 0 & 0 & S_N \end{bmatrix} \begin{bmatrix} w_0 \\ w_1 \\ w_2 \\ \vdots \\ \vdots \\ w_{N-1} \\ w_N \end{bmatrix}, \quad (1.20)
 \end{aligned}$$

where  $N$  is the number of vertical levels. Boundary Conditions have been implemented setting the first and last lines of the finite difference matrix (L.H.S.) equal to 0.

4. Eigenvalues  $\lambda$  may be found exploiting mathematical routines already implemented in programming packages.
5. Eigenvectors are found integrating Eq. 1.19 through *Numerov's* numerical method (Numerov, 1927; Numerov, 1924)

$$w_{n+1} = \left( \frac{2 - \frac{10\Delta t^2}{12}\lambda S_n}{1 + \frac{\Delta t^2}{12}\lambda S_{n+1}} \right) w_n - \left( \frac{1 + \frac{\Delta t^2}{12}\lambda S_{n-1}}{1 + \frac{\Delta t^2}{12}\lambda S_{n+1}} \right) w_{n-1}, \quad (1.21)$$

where each eigenvalue  $\lambda$  is used for computing the corresponding eigenvector  $w$ . Here,  $n$  states for the vertical level index. The first value of each eigenvector is computed as

$$w_1 = \frac{\Delta z \frac{dw}{dz}|_{z=0}}{(1 + \lambda \frac{S_1 \Delta z^2}{6})} \quad \text{with} \quad \frac{dw}{dz}|_{z=0} = -\lambda \Phi_0 \quad \left( \Phi_0 = \Phi|_{z=0} = 1 \right), \quad (1.22)$$

where  $\Phi_0$  is the surface value, equal to the modes maximum amplitude (and equal to the barotropic mode value). Here, it is set equal to 1.

6. The baroclinic Rossby deformation radii  $R_n$  are computed as in Eq. 1.12 while the vertical structure functions are obtained integrating  $S$ ,  $w$  as in Eq.1.17.

## 1.4 Thesis Objectives

In the present work, a dynamical downscaling approach has been employed for studying submesoscale features in two areas of the North Atlantic ocean. The two domains of interest respectively encompass the *Azores* archipelago, in the Azores region, and the *Bermuda* island, in the Gulf Stream region. They are characterized by different values of the 1-st mode baroclinic deformation radius.

The short-time forecasts have been carried out through SURF numerical platform (Structured and Unstructured grid Relocatable ocean platform for Forecasting), during winter period January 4<sup>th</sup>-12<sup>th</sup>, 2021. In particular, starting from a coarser "parent" model with  $1/12^\circ$  grid step, we obtain highly-resolved "child" models at  $1/48^\circ$  resolution.

Through this thesis, we aim to answer the following questions:

- Is "child" model resolution sufficient for observing the onset of submesoscale activity in the studied regions?
- Which submesoscale features may be observed through a dynamical downscaling approach in the studied regions?
- Is the deformation radius value linked to the activation of submesoscale processes?

As regards the thesis structure, in Chap. 2 we describe the regions of interest, the datasets employed, the numerical model implemented along with its set-up and parameterizations. In Chap. 3, we analyse mesoscale features in each region, obtained from "parent" model information. In Chap. 4, we show submesoscale features resulting from our high-resolution simulations. In this context, we compare "parent" and "child" models, pointing out the benefits of a high-resolution downscaling approach. In Chap. 5, we draw conclusions about the work done.

# Chapter 2

## Model and Data

### Contents

---

<b>2.1 Numerical Model</b>	<b>31</b>
2.1.1 NEMO-OCE	31
2.1.2 SURF Platform	34
<b>2.2 Regions of Interest</b>	<b>37</b>
2.2.1 The Azores Region	38
2.2.2 The Bermuda Region	38
<b>2.3 Experimental Setup</b>	<b>38</b>
2.3.1 Initial and Boundary Conditions	39
2.3.2 Atmospheric Forcing	39
2.3.3 Bathymetry and Coastlines	39
2.3.4 Tides	41
2.3.5 Model Set-Up	41

---

The downscaling simulations are performed using the structured grid component of the SURF platform (Structured and Unstructured grid Relocatable ocean platform for Forecasting) in two regions using the structured grid component of the SURF platform: one around the Azores archipelago and the other one in the Bermuda region, within the Gulf Stream area. In this chapter, we describe the simulations features, including the numerical model employed, simulation regions and datasets exploited.

## 2.1 Numerical Model

The european NEMO numerical model is exploited by both SURF platform and CMEMS forecasting system. In this section, we focuses on the ocean model NEMO, the SURF platform and the related nesting procedures.

### 2.1.1 NEMO-OCE

The NEMO numerical model (Nucleus for European Modelling of the Ocean) "*is a state-of-the-art modelling framework for research activities and forecasting services in ocean and climate sciences, developed in a sustainable way by a european consortium*" (see NEMO Community Ocean Model web page, <https://www.nemo-ocean.eu/>). Among its three major components (NEMO-OCE, NEMO-ICE and NEMO-TOP), NEMO-OCE is the one included by SURF in the downscaling process.

#### Primitive Equations for the Ocean

NEMO-OCE deals with ocean dynamics and thermodynamics, solving the 3D primitive equations for the ocean with *free surface*, under *hydrostatic*, *incompressibility* and *Boussinesq* approximations. Furthermore, a non-linear equation of state is adopted, which combines the two active tracers (temperature and salinity) with the fluid velocity. Additional assumptions made from scale considerations are the *spherical Earth approximation*, so that gravity is locally vertical, and the *thin-shell approximation*, i.e. the ocean depth is neglected compared to the earth's radius; the Coriolis terms varying with the cosine of latitude are neglected.

As regards the frame of reference, an orthogonal set of unit vectors  $(\hat{i}, \hat{j}, \hat{k})$  is chosen, linked to the Earth such that  $\hat{k}$  is the local upward vector, while  $(\hat{i}, \hat{j})$  form a horizontal vector orthogonal to  $\hat{k}$  and tangent to geopotential surfaces. The unit vectors are respectively associated to longitude, latitude and depth ( $x, y, z$  axes).

The variables involved are: velocity  $\vec{U} = (u, v, w)$ , potential temperature  $\theta$ , salinity  $S$ , pressure  $p$  and density  $\rho$ . Thus, the overall Equation (Eq.) set assumes the following form (cit - NEMO MANUAL):

- Momentum balance Eq.

$$\frac{\partial \vec{U}_h}{\partial t} = - [(\nabla \times \vec{U}) \times \vec{U} + \frac{1}{2} \nabla(U^2)]_h - \vec{f} \times \vec{U}_h - \frac{1}{\rho_0} \nabla_h p + D^U + F^U \quad (2.1)$$

## 2.1. Numerical Model

---

where the subscript  $n$  stands for the horizontal vector, i.e. projected on  $(\hat{i}, \hat{j})$ ;

- Heat and salt conservation Eq.s

$$\frac{\partial \theta}{\partial t} = -\nabla \cdot (\theta \vec{U}) + D^\theta + F^\theta \quad , \quad (2.2)$$

$$\frac{\partial S}{\partial t} = -\nabla \cdot (S \vec{U}) + D^S + F^S \quad ; \quad (2.3)$$

- Hydrostatic balance

$$\frac{\partial p}{\partial z} = -\rho g \quad ; \quad (2.4)$$

- Continuity Eq. (incompressibility hypothesis)

$$\nabla \cdot \vec{U} = 0 \quad ; \quad (2.5)$$

- Eq. of state

$$\rho = \rho(\theta, S, p) \quad . \quad (2.6)$$

In the above set,  $\rho_0$  is a reference density,  $\vec{f} = 2\Omega\hat{k}$  the coriolis acceleration and  $g$  the gravitational acceleration module.  $F^U$ ,  $F^\theta$  and  $F^S$  are the surface forcing terms while  $D^U$ ,  $D^\theta$  and  $D^S$  are the parameterisations of subgrid scale physics, i.e. non-resolved turbulence defined through closure schemes.

### Discretization Method

The above equation set is implemented in NEMO through finite difference methods.

The *Leap-Frog* scheme is the time stepping scheme used for processes as momentum and tracer advection, pressure gradient and Coriolis terms, but not for diffusion terms. This scheme is widely used for advection processes in low-viscosity fluids. It is a three-level centered explicit time scheme that achieves second-order accuracy with just one right hand side evaluation per time step. Moreover, it does not artificially damp linear oscillatory motion nor does it produce instability by amplifying the oscillations. However, divergence of odd and even time steps may occur. To prevent it, the leap-frog scheme is associated with a Robert-Asselin time filter which acts as a slight time smoothing.

For diffusion terms, a forward (explicit) time differencing scheme is used,

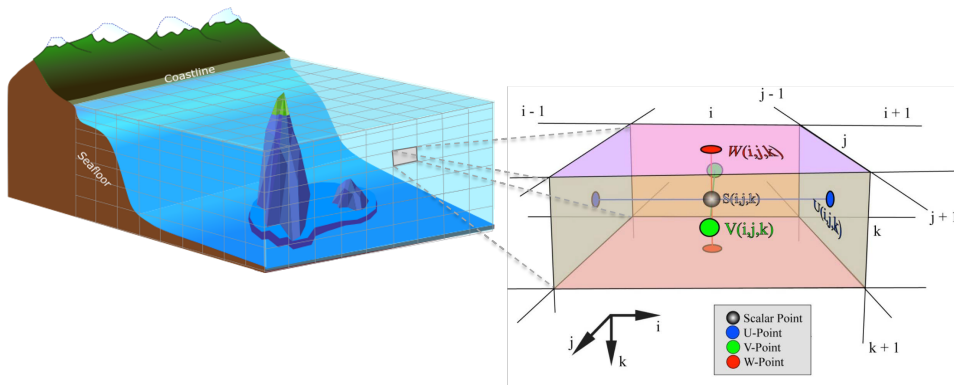


**FIGURE 2.1:** Arrangement of variables using the staggered Arakawa C-type grid, as in NEMO-OCE model (courtesy of Dr. Francesco Trotta).  $S$  indicates scalar points where scalar quantities are defined;  $U$ ,  $V$  and  $W$  indicate vector points where the three velocity components are defined. Indices  $(i,j,k)$  respectively stands for longitude, latitude and depth grid indices.

which implies stronger constraints to achieve stability especially for vertical diffusion terms. In the last case, a backward (implicit) time differencing scheme may be employed to overcome stability issues, although this scheme is rather time consuming.

NEMO-OCE uses time-splitting technique, too, i.e. two different time steps are employed to separately integrate barotropic and baroclinic modes of motion. This way, the (faster) barotropic mode is integrated with smaller time step respect to the (slower) baroclinic mode, containing the computational expense without losing stability.

As regards the spatial discretization, a three-dimensional Arakawa C-type grid is used for discretizing the spatial domain (Fig. 2.1). Variables are defined on staggered grids: the free surface, density, and active tracers are located at the center of the cell (T-grid), horizontal  $u$  and  $v$  velocities are located at the west/east and south/north edges of the cell (U-grid and V-grid); vertical velocity  $w$  is located at the bottom and top interfaces of cell (W-grid). In the horizontal direction, the NEMO model uses a structured curvilinear orthogonal grid, while in the vertical direction it is possible to choose among geopotential  $z$ -coordinate system, terrain-following  $\sigma$ -coordinate system or a mixture of the two.

Further information about NEMO model and its numerical schemes may be

found within *NEMO ocean engine* manual ([Climate Modelling Center, 2022](#)).

### 2.1.2 SURF Platform

SURF (Structured and Unstructured grid Relocatable ocean platform for Forecasting) is a numerical platform for high-resolution short-time forecast of hydrodynamic and thermodynamic fields that characterise ocean circulation ([Trotta et al., 2016; 2021](#)). It is designed to be embedded into any region of a large scale ocean prediction system via a robust nesting methodology. The SURF workflow connects numerical integration codes to several pre- and post-processing procedure, making each platform component easy to deploy in a limited region which is part of the parent model domain in which SURF is nested.

#### Nesting Procedure

Through SURF one obtains a high-resolution nested model, called *child*, from a coarser nesting one, called *parent*, exploiting a downscaling process. The increasing resolution may involve both time and space dimensions. The nesting model may be a coarse OCGM (Ocean General Circulation Model) or an already nested model, so that multiple nesting is allowed. For the nesting, Boundary and Initial Conditions are required from the parent model, that is fields as horizontal velocity  $(U, V)$ , temperature  $T$ , salinity  $S$  and free surface height  $\eta$ . Furthermore, the atmospheric forcings has to be provided, along with high-resolution bathymetry dataset and detailed coastal geometry. The physical parameterizations must be set (e.g. sub-grid scale physics), but they may differ from parent to child model.

To obtain high-resolution initial and boundary conditions, the parent model is interpolated onto the new child grid. Horizontal and vertical interpolation is a key feature of the nested model initialization procedure. SURF uses a method developed by [Dominicis et al. \(2014\)](#), in which the coarser-resolution ocean fields are extrapolated using the Sea-Over-Land (SOL) procedure. This routine uses a diffusive boundary layer approach that extrapolates the field values on the areas near the coastline where the parent model solutions are not defined. The SOL procedure iteratively computes the ocean quantities on the land grid-points, so that these quantities can be interpolated on the child grid. This also applies to atmospheric fields in order to avoid land contaminations near the land-sea boundaries. After SOL has been applied,

a bilinear interpolation method is used. A simple linear interpolation is used for vertical interpolation.

### Discretization

In the horizontal direction, the model employs a curvilinear orthogonal grid. In the vertical direction, a stretched geopotential z-coordinate system is used. Layers are distributed along the water column with increasing resolution approaching the resting ocean surface, to better resolve dynamics in surface and intermediate layers. Thus, given a vertical level indexed  $k$ , the corresponding depth is given by

$$z(k) = h_{sur} - h_0 k - h_1 \log \left[ \cosh \left( \frac{k - h_{th}}{h_{cr}} \right) \right] , \quad (2.7)$$

where  $h_{cr}$  is the grid stretching factor and  $h_{th}$  the approximate model level at which maximum stretching occurs. Parameters  $h_{sur}$ ,  $h_0$  and  $h_1$  depend on  $h_{cr}$ ,  $h_{th}$ , the number of vertical levels, the maximum depth and the top layer minimum thickness. Furthermore, partial cell parameterisation is employed, which means bottom layer thickness varies as a function of position in order to fit the real bathymetry.

Lastly, the time step is limited by the Courant-Friedrichs-Lewy (CFL) criterion, to ensure numerical stability.

### Numerical Schemes and Parameterizations

Going further about numerical schemes, the momentum advection is implemented through an Energy and ENstrophy conserving (EEN) scheme which conserves both potential enstrophy of horizontally non-divergent flow and horizontal kinetic energy. Tracers advection employs a Monotonic Upstream-centered Scheme for Conservation Laws (MUSCL).

Mesoscale turbulence is resolved but sub-grid scale physics needs parameterization. Thus, vertical submesoscale turbulence employs the Pacanowski-Philander vertical mixing parameterization, in which the vertical eddy coefficients are function of the local Richardson number. Horizontal submesoscale turbulence may be parameterized through lateral laplacian or bilaplacian momentum diffusive operators.

### Boundary Conditions

The coarse-grid parent model provides initial and lateral Boundary Conditions (BCs) to the fine-grid child model. Parent BCs enter at lateral open

## 2.1. Numerical Model

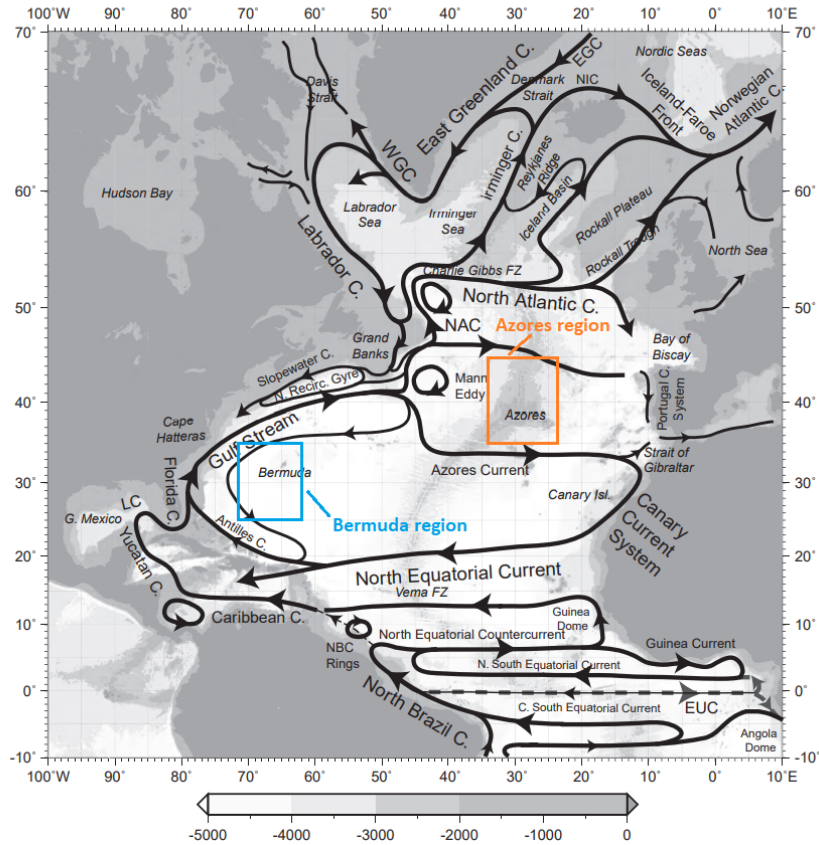


**FIGURE 2.2:** Wind-driven surface circulation schematics in the North Atlantic Ocean, from [Talley et al. \(2011\)](#). The two regions of interest are found in coloured boxes.

boundaries, where the Flather and flow relaxation conditions are applied. The first one is a radiation condition on the normal, depth-mean transport across open boundaries. The second one is a relaxation of child model fields to externally-specified parent values, over a zone next to the edge of child domain. Tidal barotropic forcing (ssh and velocity) can also be added to the barotropic velocity at the open boundaries. To preserve the total transport after horizontal and vertical interpolation, an integral constraint method is applied ([Pinardi et al., 2003](#)).

Non-linear quadratic friction is applied at sea bottom, while the no-slip conditions are imposed at closed lateral boundaries

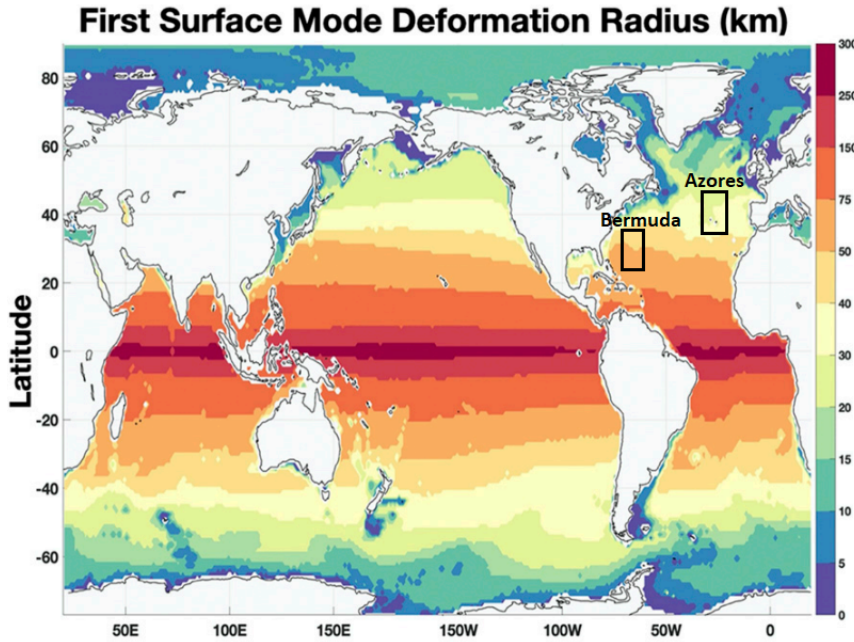


**FIGURE 2.3:** Map of the first surface mode baroclinic deformation radius according to [LaCasce et al. \(2020\)](#). The regions of interest are found in boxes.

## 2.2 Regions of Interest

Two high-resolution simulations are performed in the context of this thesis work, each of them in a distinct region of area  $10^\circ \times 10^\circ$ . Hereafter, the two will be addressed as the *Azores* and *Bermuda* regions.

The two regions have been chosen based on mesoscale dynamics. In fact, they are united by the presence of very evident mesoscale currents. As visible in [Fig. 2.2](#), the Bermuda region includes part of the *Gulf Stream System* while the Azores one includes part of the *Azores current*. These are branches of the North Atlantic Subtropical Gyre, which both constitute a *jet current* in the corresponding area, though they differ in terms of intensity and direction ([Talley et al., 2011](#)). Furthermore, the two regions are characterized by different values of the *baroclinic deformation radius* as computed in [LaCasce et al. \(2020\)](#) ([Fig. 2.3](#)).

All these features are important for the development of submesoscale activity, as discussed in [Chap. 1](#).

## 2.3. Experimental Setup

---

### 2.2.1 The Azores Region

The *Azores* region encompasses the Azores archipelago, going from  $35^{\circ}N$ ,  $33.5^{\circ}W$  to  $45^{\circ}N$ ,  $23.5^{\circ}W$ . It includes the Azores current, a zonal jet resulting from the eastward splitting of the Gulf Stream, which extends eastward toward the Strait of Gibraltar (Fig. 2.2, orange box). Here, a small amount of surface water flows into the Mediterranean Sea, which makes this a key region associated to the Mediterranean inflow (Talley et al., 2011).

### 2.2.2 The Bermuda Region

The *Bermuda* region extends from  $25^{\circ}N$ ,  $72^{\circ}W$  to  $35^{\circ}N$ ,  $62^{\circ}W$ . It includes the Bermuda island and part of the Gulf Stream System (Fig. 2.2, light blue box). In particular, it includes the so-called *Gulf Stream recirculation*, a mean westward surface flow just south of the Gulf Stream. Together, the Gulf Stream and its recirculation form the *Gulf Stream recirculation gyre*. It is likely driven by the Gulf Stream's instability which forces westward flow on its flanks. These features make the region important in terms of water transport which becomes larger going offshore (Talley et al., 2011).

## 2.3 Experimental Setup

Both simulations are carried out during time period from January 4<sup>th</sup>, 2021 to January 12<sup>th</sup>, 2021. The period is chosen since submesoscale activity appears to be stronger during winter months according to literature (Ajayi et al., 2020; Mensa et al., 2013). The first 3 days serve as *spin-up* period and results are analysed starting from January 7<sup>th</sup>. The *spin-up period* is defined as the time necessary by the child ocean model to reach a steady state value for the volume average kinetic energy, starting from initial and lateral boundary conditions interpolated from the parent model (Simoncelli et al., 2011).

Through the downscaling procedure, the child model results to be four times finer than the parent one. In fact, we go from a coarser global OGCM with  $1/12^{\circ}$  resolution, provided by CMEMS, to a finer  $1/48^{\circ}$  resolution nested model obtained through SURF. This means the grid step becomes  $\Delta \approx 2.3km$ , from a starting value of  $\approx 9km$ .

In the following subsections, the datasets employed for Initial and Boundary

Conditions (including atmospheric forcings) will be described, along with the bathymetry dataset and the parameters used to set-up both simulations.

### 2.3.1 Initial and Boundary Conditions

Ocean Initial and lateral Boundary Conditions are provided by Copernicus Marine Environment Monitoring Service (CMEMS, [Le Traon et al. \(2019\)](#)). In particular, we have employed the operational CMEMS-global analysis and forecast daily mean product (GLOBAL\_ANALYSIS\_FORECAST\_PHY\_001\_024), from which we download temperature, salinity, sea surface height ( $\eta$ ) and total velocity (U,V) fields. The CMEMS model is defined on a regular grid with a horizontal resolution of  $1/12^\circ$  ( $\approx 8$  km) and 50 vertical-levels ranging from 0 to 5500 meters ([Chune et al., 2021](#)). It results from the Operational Mercator global ocean analysis and forecast system at  $1/12^\circ$ , which provides 10 days of 3D global ocean forecasts updated daily, starting from January 1<sup>st</sup>, 2016.

### 2.3.2 Atmospheric Forcing

Atmospheric Boundary Conditions are obtained exploiting ERA5 datasets by the European Centre for Medium-range Weather Forecasts (ECMWF, see [ECMWF-ERA5 website](#)). The data cover the Earth on a  $30km$  grid and resolve the atmosphere using 137 levels from the surface up to  $80km$  height. ERA5 combines vast amounts of historical observations into global estimates using advanced modelling and data assimilation systems. In particular, it is produced using 4D-Var data assimilation and model forecasts from the ECMWF Integrated Forecast System (IFS). The air-surface fluxes of momentum, water, and heat are computed using specific bulk formulas, as described by [Pettenuzzo et al. \(2010\)](#) using the x-hours, 0.25 horizontal-resolution ERA5 data.

### 2.3.3 Bathymetry and Coastlines

The bathymetry dataset is provided by General Bathymetric Chart of the Oceans (GEBCO) organization (see [website](#)). GEBCO\_2014 dataset, the version employed here, consists of a global terrain model for ocean and land at  $30arcsec$  interval, approx. 900 m ([Becker et al., 2009](#)). The bathymetry

### 2.3. Experimental Setup

---

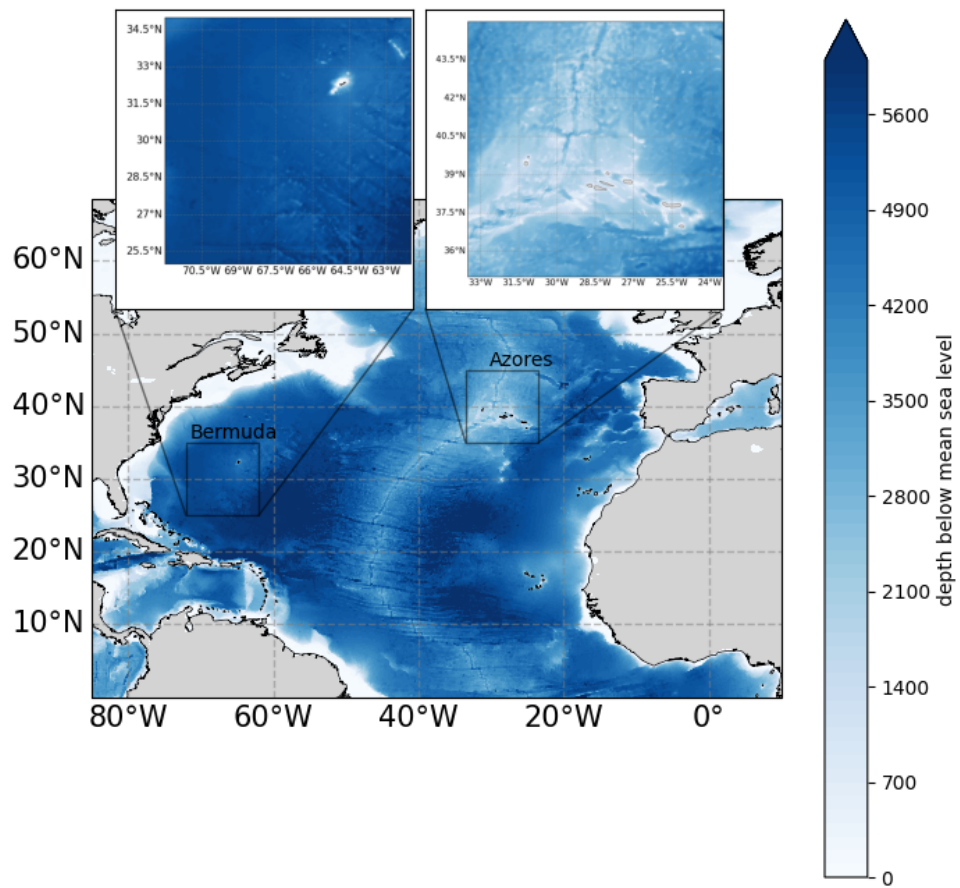


**FIGURE 2.4:** Bathymetry contour map of the North Atlantic Ocean as obtained from GEBCO datasets at 30 arcsec resolution. The two (black) boxes delineate the boundaries of the nested domains.

in the regions of interest is shown in Fig. 2.4.

The coastline dataset used in SURF comes from the National Oceanic and Atmospheric Administration (NOAA) agency. It is called GSHHG (Global Self-consistent, Hierarchical, High-resolution Geography Database) as in [Wessel et al. \(1996\)](#).

### 2.3.4 Tides

Tides are included in SURF simulations as Boundary Condition. Tidal currents are provided to the child model from TPXO8-atlas dataset, by Oregon State University, USA (see TPXO [website](#)). TPXO is a series of fully-global models of ocean tides, which reproduces the Laplace Tidal Equations and altimetry data. The models are based on updated bathymetry and data assimilation, obtained through OTIS software which implements methods described in details by [Egbert et al. \(1994\)](#) and further by [Egbert et al. \(2002\)](#). In particular, TPXO8-atlas combines a basic global solution (i.e. TPXO8, obtained at  $1/6^\circ$  resolution) and high-resolution (HR) local solutions. Since TPXO8-atlas keeps higher resolution of most HR solutions rather than averaging them on coarser grid, tidal predictions for coastal areas are significantly improved.

Here, we employ the following tidal components: lunar diurnal "K1" and "O1", solar diurnal "P1", larger lunar elliptic diurnal "Q1", lunisolar semidiurnal "K2", principal lunar semidiurnal "M2", larger lunar elliptic semidiurnal "N2", principal solar semidiurnal "S2", shallow water overtides of principal lunar constituent, "M4".

### 2.3.5 Model Set-Up

In Fig. 2.5 the distribution of vertical levels is shown, comparing the parent and child models, with a focus on the first surface levels. The distribution follows Eq. 2.7. To notice, while all the distribution parameters are defined within the parent model, within the child one they are computed starting from  $dz_{min}^w$  and  $h_{max}$  values, i.e. the minimum vertical spacing and the region maximum depth.

The two simulations have been set-up in the very same way, so that the results between the two regions are comparable. Relevant coefficients and parameters for setting-up the model may be found in Tab. 2.1. As regards

### 2.3. Experimental Setup

---

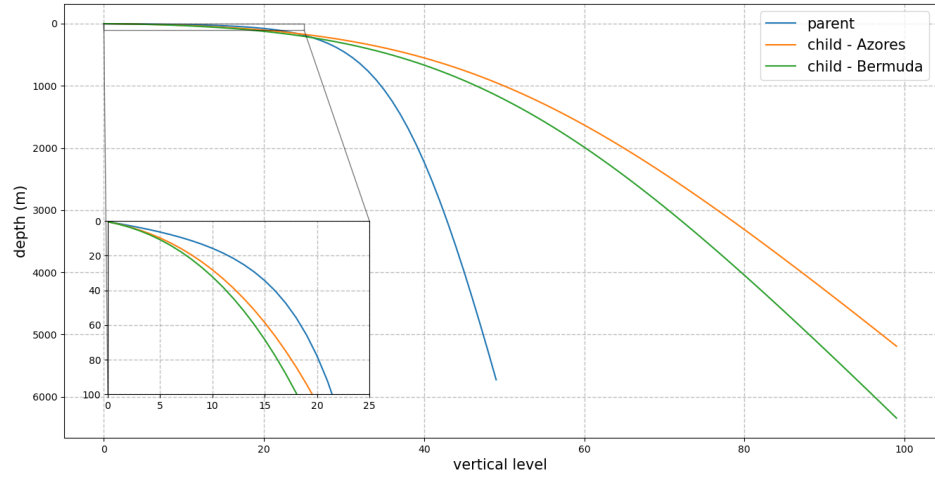


**FIGURE 2.5:** *Distribution of vertical levels in child and parent models, with focus on the first 100 m (box).*

turbulence and sub-grid scale physics, the horizontal eddy viscosity is parameterized through the lateral bilaplacian diffusive operator (coeff $<0$ ) in the parent model. Differently, the lateral laplacian diffusive operator (coeff  $>0$ ) is used in the child one. Horizontal eddy diffusivity is parameterized through the laplacian operator for both parent and child models. Lastly, vertical turbulence is implemented through the Turbulent Kinetic Energy (TKE) mixing scheme in the parent model, while through the Pacanowski-Philander (PP) mixing scheme in the child one.

PARAMETERS	PARENT	AZORES CHILD	BERMUDA CHILD
<b>Time</b>			
time date	2016 - now	Jan 4 - 12, 2021	Jan 4 - 12 2021
spinup time	-	3 days	3 days
$\Delta t_{baroclinic}$	360 s	100 s	100 s
Courant num.	-	$C \leq 0.8$	$C \leq 0.8$
output	daily	hourly	hourly
<b>Horizontal grid</b>			
longitude $\lambda$ ( $^{\circ}$ W)	global	$33.5 \div 23.5$	$72 \div 62$
latitude $\phi$ ( $^{\circ}$ N)	global	$35 \div 45$	$25 \div 35$
$\Delta\lambda, \Delta\phi$	$0.083^{\circ}$	$0.021^{\circ}$	$0.021^{\circ}$
$\Delta x, \Delta y$	$\sim 9.0km$	$\sim 2.3km$	$\sim 2.3km$
$n_x \times n_y$	$4320 \times 2041$	$480 \times 480$	$480 \times 480$
<b>Vertical grid</b>			
$n_z$	50	100	100
$h_{cr}$	-	30	30
$h_{th}$	-	50	50
$dz_{min}^w$ (m)	-	1.0	1.0
$h_{max}$ (m)	5727.9	5188.0	6344.1
<b>Sub-grid physics</b>			
hor. viscosity	$-1.25 \times 10^{10}$ $m^4/s^2$	$25.0 m^2/s$	$25.0 m^2/s$
hor. diff. ( $m^2/s$ )	100	25.0	25.0
vert. mixing	TKE param.	PP param.	PP param.
vert. visc. ( $m^2/s$ )	$1.0 \times 10^{-4}$	$1.2 \times 10^{-6}$	$1.2 \times 10^{-6}$
vert. diff. ( $m^2/s$ )	$1.0 \times 10^{-5}$	$1.0 \times 10^{-7}$	$1.0 \times 10^{-7}$
EVD coeff. ( $m^2/s$ )	10	10	10
<b>Bottom friction</b>			
drag coeff.	$1.0 \times 10^{-3}$	$1.0 \times 10^{-5}$	$1.0 \times 10^{-5}$
bottom TKE ( $m^2/s^2$ )	-	$2.5 \times 10^{-3}$	$2.5 \times 10^{-3}$

**TABLE 2.1:** *Child model configuration as set in the two experiments within Azores and Bermuda regions. When the values are defined and known, parent and child models are compared.*

## Chapter 3

# Mesoscale Analysis in the Azores and Bermuda Regions

### Contents

---

<b>3.1 Horizontal Features</b> . . . . .	<b>45</b>
<b>3.2 Vertical Insight</b> . . . . .	<b>49</b>

---

Through the following sections, we aim to give the reader an overview about mesoscale features in the two regions of interest, gained from the "parent" global model information. Mesoscale features are compared between January 7<sup>th</sup> and 12<sup>th</sup> 2021, i.e. the first simulation day after the spin-up period and the last simulation day.

We analyse horizontal fields, such as currents and temperature, and vertical properties as temperature and salinity profiles. In particular, we focus on horizontal fields within the surface Mixed Layer, at 10 m depth. Furthermore, special attention is given to the vertical stratification analysis. This is studied through the Mixed-Layer Depth field and the Brunt-Väisälä frequency vertical profile. A zonal transect is shown, too, in order to give an idea of vertical velocities magnitude and pycnoclines disposition. In this context, we try to understand if Mixed-Layer Instability plays a role among the restratification processes which seem to take place during the simulation period in both regions. This would provide a connection between mesoscale features and submesoscale currents.

### 3.1 Horizontal Features

As discussed in the previous chapter, the two regions are characterized by great mesoscale activity, due to the presence of horizontal jet currents in the nearby. This is evident from Fig. 3.1, where the daily mean current field is shown at 10 m depth at the last simulation day, in the two areas of interest (bordered by black boxes). At first glance, one may immediately notice the Gulf Stream meanders and rings (Fig. 3.1a). A big amount of mesoscale eddies is present in both regions, though in the azores one there seems to be smaller mesoscale eddies (Fig. 3.1b). This is coherent with the baroclinic deformation radius value in the two areas: as in the Azores one it assumes smaller values, mesoscale eddies have smaller length scales.

#### Currents, Temperature and Relative Vorticity

As regards daily mean currents, temperature and relative vorticity, we show the horizontal fields nearly 10 m deep. This is considered significative for studying horizontal features inside the Mixed-Layer, as here important submesoscale processes may take place. In Figs 3.2 and 3.3 the fields evolution is shown in both regions, comparing values for Jan 7<sup>th</sup> and 12<sup>th</sup>, 2021. In the Azores region, many mesoscale vortices persist during the simulation days especially in the northern side, as it appears from the current fields (Fig. 3.2a). However, only few of them seem to be outlined by a clear temperature structure (Fig. 3.2b). In the southern part, one may notice the evolution of meanders into vortices. Here, the ocean temperature increases, so that it ranges from about 12 to 22 °C in the whole domain, as expected due to the latitude variation. After all, temperature (Fig. 3.2b) and relative vorticity (Fig. 3.2c) fields remain very similar during the simulation time-period.

In the Bermuda region, meanders and vortices seem to persist along the whole domain. Differently from the Azores case, their length scales seem to be greater, from a qualitative point of view (Fig. 3.3a). Furthermore, by looking at the temperature field one may better identify the signature of meanders and big vortices (Fig. 3.3b). Being the region further southward, temperatures are larger, ranging from about 18 to 28 °C. As a point of interest, in this region, temperature (Fig. 3.3b) and relative vorticity (Fig. 3.3c)

### 3.1. Horizontal Features

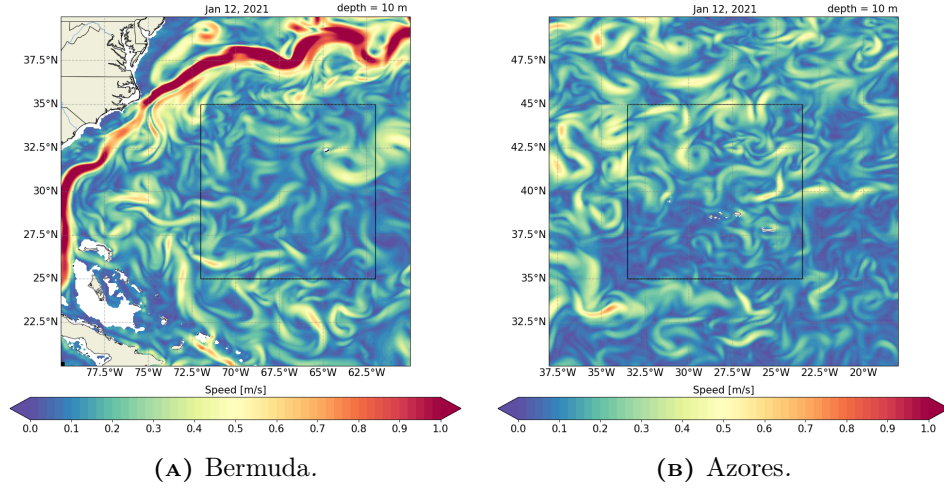


**FIGURE 3.1:** Daily mean current speed at 10 m depth from the parent CMEMS-global model, in the Bermuda (a) and Azores (b) regions. Black boxes delineate the boundaries of the two nested domains.

fields seem to present more significant local differences than the Azores ones. This seems to be true especially where big vortices persist.

All things considered, it seems that the horizontal mesoscale features remain quite similar during the simulation days in the Azores region, as expected due to the short time period. While in the Bermuda region currents seems to remain quite unchanged at a first glance, temperature and vorticity fields reveal mesoscale variations. This is coherent with the deformation radius value, which is higher in the Bermuda domain. Here, we expect wider mesoscale vortices which may influence the temperature field faster and longer through greater heat transport.

Finally, it can be noted that in both cases the presence of the islands does not seem to influence mesoscale flows a lot.

Chapter 3. Mesoscale Analysis in the Azores and Bermuda Regions

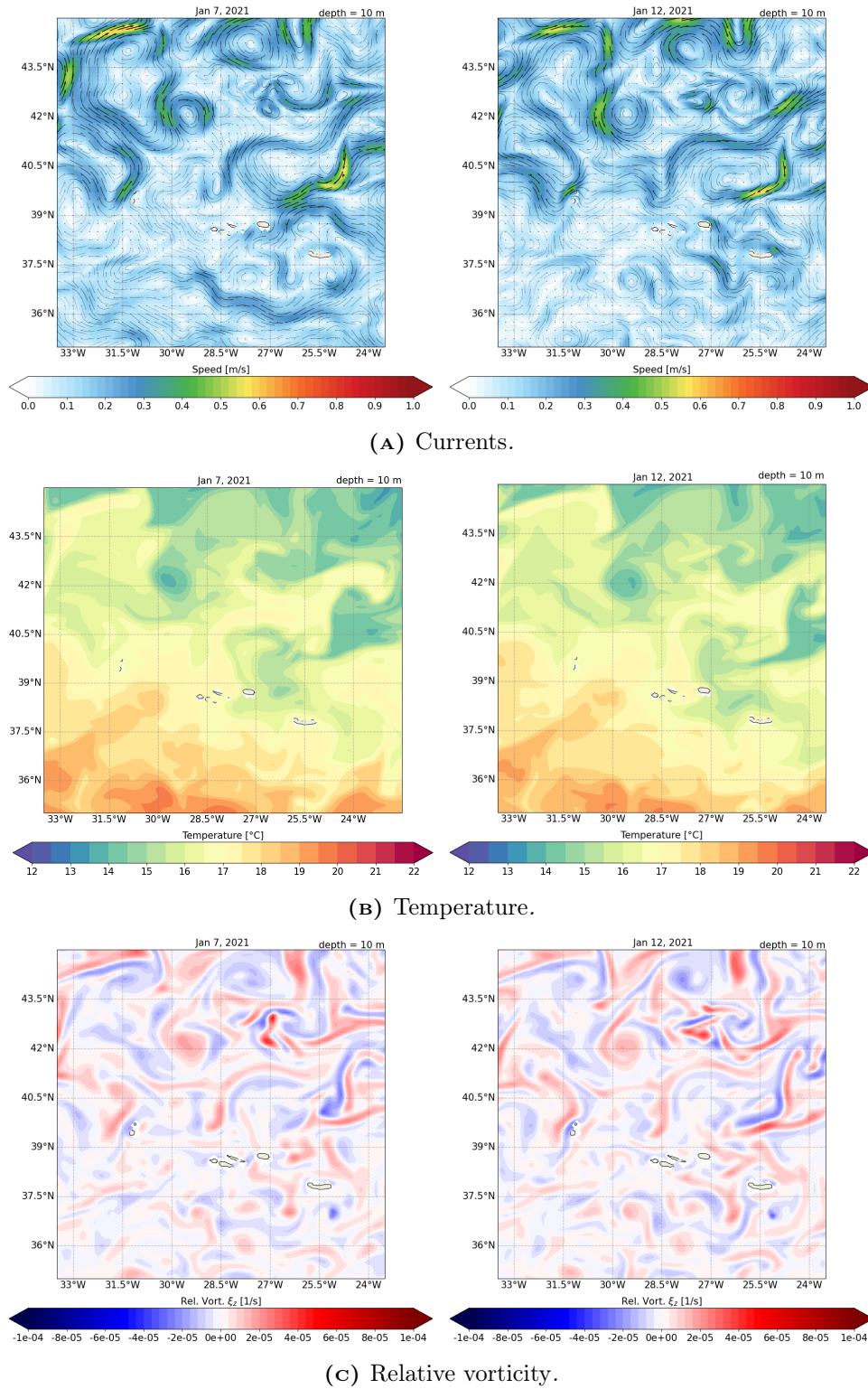
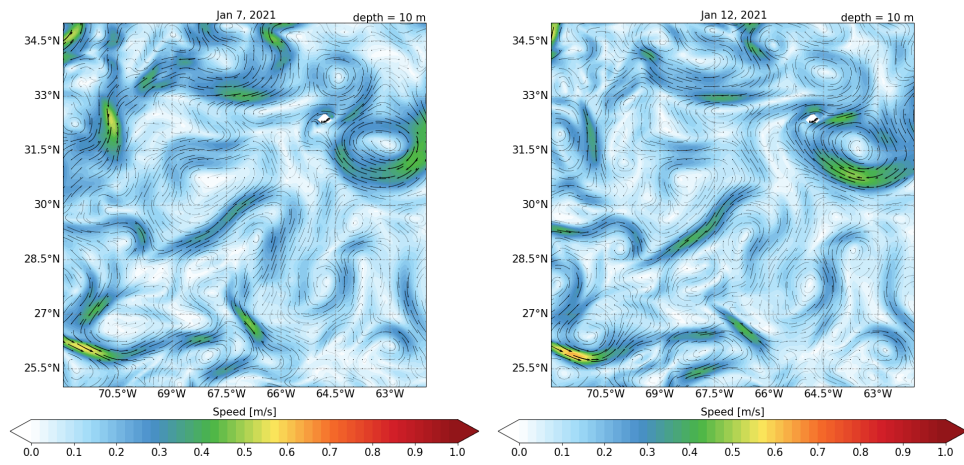
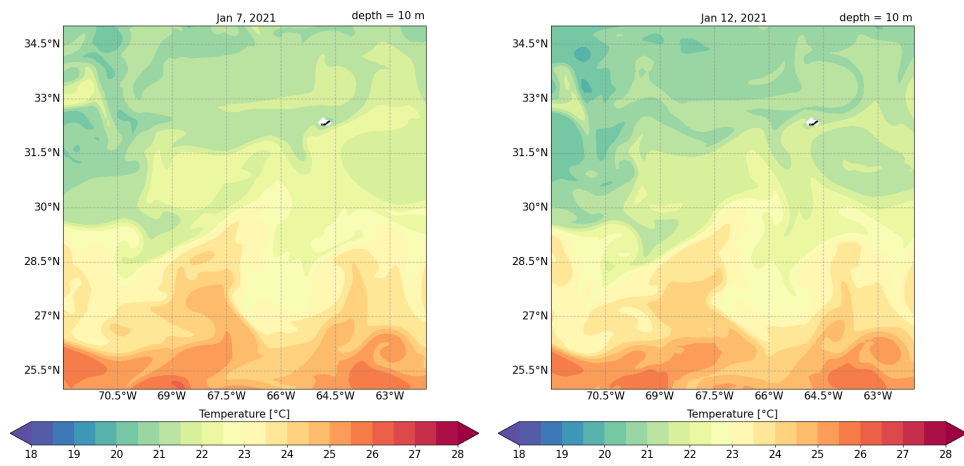


**FIGURE 3.2:** Daily mean currents (a), temperature (b) and relative vorticity (c) fields at 10 m depth in the Azores region, on January 7 (left panels) and 12 (right panels), 2021.

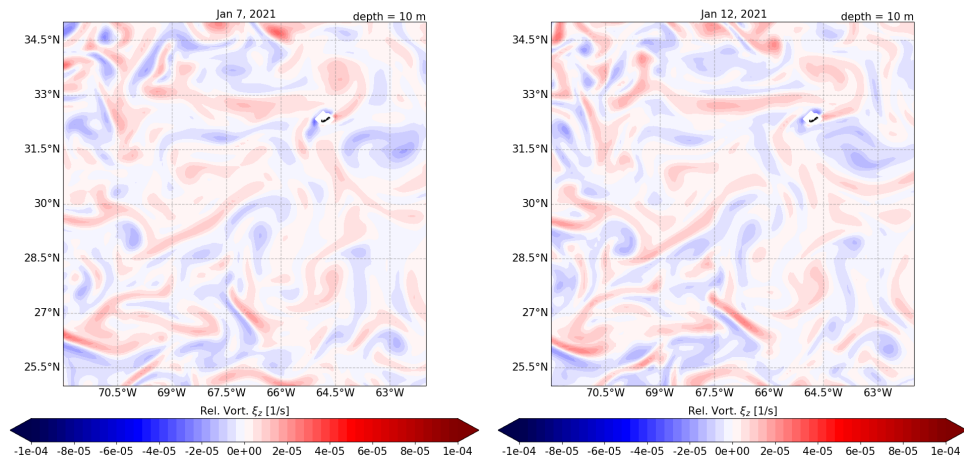
### 3.1. Horizontal Features



(A) Currents.



(B) Temperature.



(C) Relative vorticity.

**FIGURE 3.3:** Daily mean currents (a), temperature (b) and relative vorticity (c) fields at 10 m depth in the Bermuda region, on January 7 (left panels) and 12 (right panels), 2021.

## 3.2 Vertical Insight

We discuss seawater vertical properties in the two regions of interest, since the eventual onset of submesoscale processes is strongly related to restratification in the upper layers. Thus, a vertical insight of the water column structure evolution takes on particular importance.

In Fig. 3.4, the mean vertical salinity and temperature profiles are shown, along with the Brunt-Väisälä (BV) frequency squared. BV frequency is obtained as in Chap. 1 from the density profile averaged over the region, which is computed from vertical mean temperature and salinity as in Fofonoff et al. (1983). Henceforth, we will use simply "BV freq." for meaning the Brunt-Väisälä frequency squared. The profiles are compared between the Azores and Bermuda regions on Jan 7, 2021, to give an idea of the regions initial vertical structure. The profiles significantly differ up to about 1000 m depth for salinity, and 2000 m depth for temperature. Both surface temperature and salinity are far greater in the Bermuda region (Fig. 3.4, left panel). Here, there is a greater excursion within the first 1000 m, leading to strong density gradients as outlined by the sharper local maxima and minima in the BV freq. profile (Fig. 3.4, right panel). Differently, the BV freq. shape seems to be more gentle in the Azores region as the excursion is minor and density gradients are lower. Below 1000 m depth, the two BV freq. profiles tend to coincide as the vertical stratification becomes typical of the North Atlantic ocean interior. Thus, we may expect restratification processes are important in the upper hundreds meters in both regions, during our simulation period. However, in the Bermuda region it may take a while, needing more time than the few simulation days for being observed. This would be coherent with the role of Bermuda wider mesoscale eddies in perturbing the density field at longer time scales.

To better appreciate the vertical properties evolution in the ocean upper layers, we directly compare BV freq. profiles on Jan 7 and 12, 2021 in both regions, along with the daily Mixed-Layer Depth (MLD) (Fig. 3.5). From the BV freq. evolution, it seems restratification processes really takes place in the first few hundreds meters in both regions, counteracting the density gradients while smoothing the BV freq. vertical shape (Fig. 3.5a). In particular, it seems the thickness of the surface mixed-layer remains quite constant. In this context, we refer to the mixed-layer thickness as the surface layer where properties are clearly mixed, distinguishing it from the MLD

### 3.2. Vertical Insight

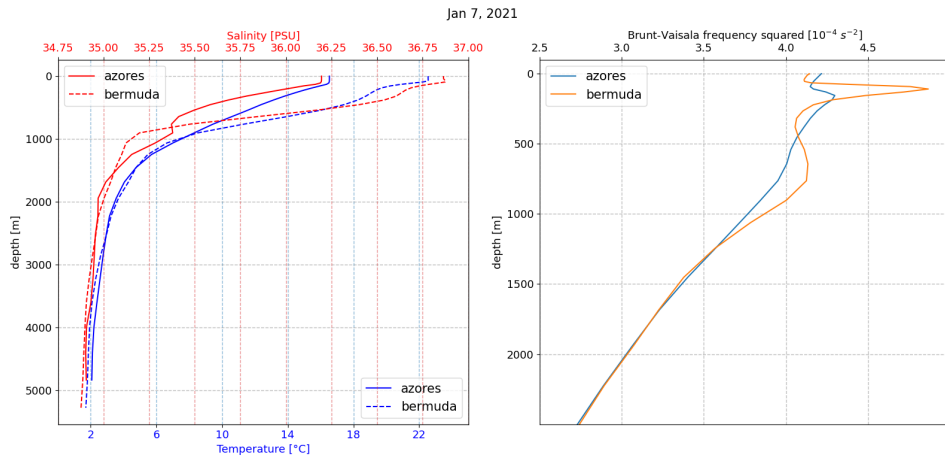


**FIGURE 3.4:** Vertical profiles of salinity, temperature (left panel) and Brunt-Vaisala frequency squared (right panel): comparison between Azores and Bermuda regions on Jan 7, 2021.

which is little larger. In fact, within the parent global model the MLD is defined as the depth where the density increase compared to density at 10 m depth corresponds to a temperature decrease of  $0.2^\circ\text{C}$  in local surface conditions (Chune et al., 2021). The profile peak, corresponding to pycnoclines stacking typical of the layers just below the surface mixed-layer, remains well distinct from the upper nearly-constant part where properties are well mixed, during the whole simulation period. Coherently, the mixed-layer thickness should remain quite unchanged during the simulation days as its variability is known to be seasonal, related to heat exchange and wind variability. However, if we observe the evolution of the daily MLD averaged over the all area, there is a clear trend (Fig. 3.5b), with greater variations in the Azores. This might mean that MLD variations during simulation days do not influence the long-term mean thickness of the mixed-layer, as they take place only in its bottom part where properties begin to assume a clearer structure. These kind of MLD fluctuations of order  $O(\text{days})$  may reveal the presence of Mixed-Layer Instability (MLI), as deeply discussed by Boccaletti et al. (2007), which might play a role among the restratification processes. Lastly, the fluctuations magnitude might be related to the deformation radius value, as it is quite different between the two regions.

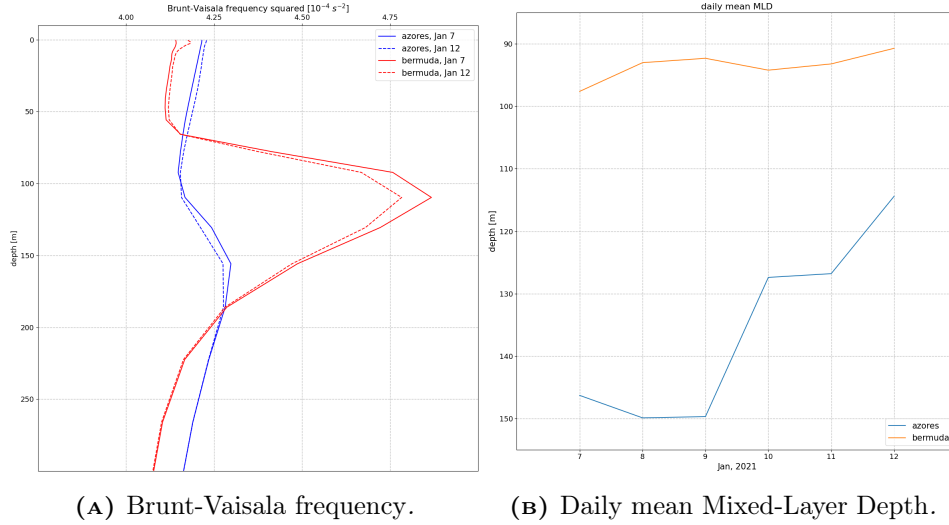


**FIGURE 3.5:** *Brunt-Vaisala frequency squared comparison on Jan 7 and 12, 2021 in both regions, with focus on the ocean upper layers (a). Temporal evolution of the daily mean Mixed-Layer Depth during simulation period from 7 to 12 January, 2021 (b).*

### Mixed-Layer Depth and Vertical Velocities

To understand if MLI really occurs during the simulation days, we now analyse MLD evolution along the two regions (Figs 3.6 and 3.7). Furthermore, we show a zonal transect of vertical velocities and pycnoclines, since MLI is related to significantly increasing vertical velocities, as already discussed in Chap. 1.

In both regions, there are visible MLD decreases, which are more consistent in the Azores one (Fig. 3.6a). While in the Azores the MLD variations are clearly visible along the whole domain, in the Bermuda area there are slight but appreciable variations especially in the south-eastern part (Fig. 3.7a). Values are coherent with Fig. 3.5b.

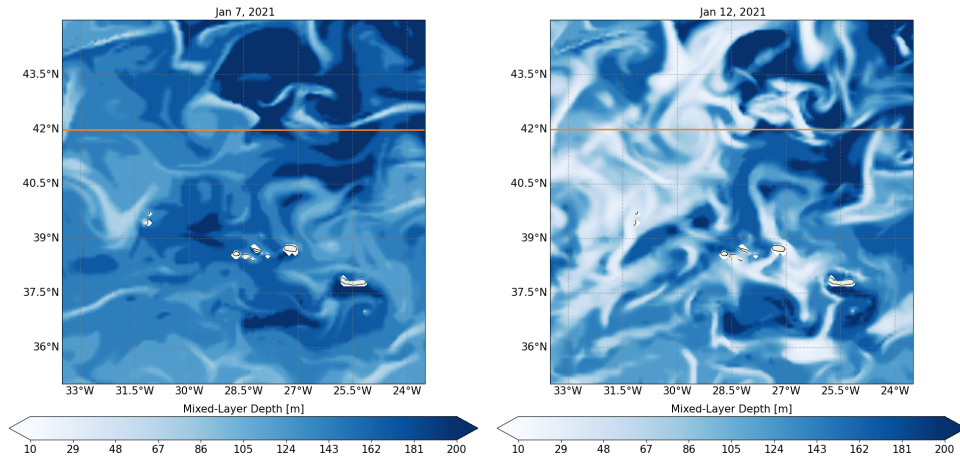
The MLI presence might be confirmed by large variations of vertical velocities during the simulation days. For this purpose, the zonal cross-section (transect) is chosen based on the latitude at which large MLD variability shows up, i.e.  $42^\circ \text{N}$  for the Azores (Fig. 3.6b) and  $28.5^\circ \text{N}$  for the Bermuda region (Fig. 3.7b). As regards the Azores, there is a tendency of smoothing the upper pycnoclines typical of restratification, which does not appear in the Bermuda region. This is coherent with the previously discussed idea that in

### 3.2. Vertical Insight

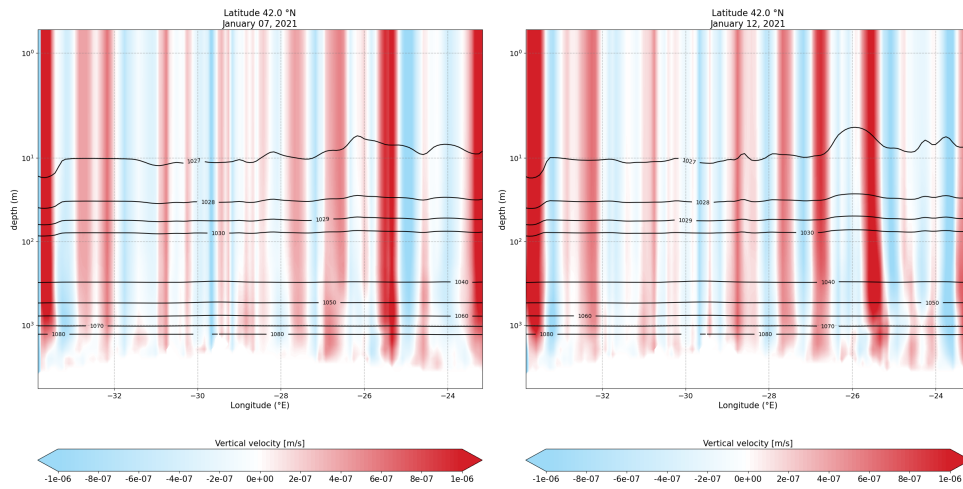
---

the Bermuda region restratification processes might take longer. The zonal structure of the vertical velocity field is quite clear, with higher values where the pycnoclines show local maxima or minima. Vertical velocities are of order  $O(10^{-6} \div 10^{-7})$ , computed from horizontal ones through the continuity equation. However, the field structure seems to be very similar throughout the simulation, with only slight increases near pycnocline extremants. Thus, the parent vertical velocity field does not seem decisive for determine the effective presence of MLI during the restratification processes. This might be due to the parent low resolution, which may not allow the detection of submesoscale vertical currents generated by MLI.

In next chapter, through our high-resolution model we try to assess MLI occurrence during simulation days and its eventual contribution to the restratification processes. This might provide a connection, through MLI, between mesoscale features and the onset of submesoscale activity.



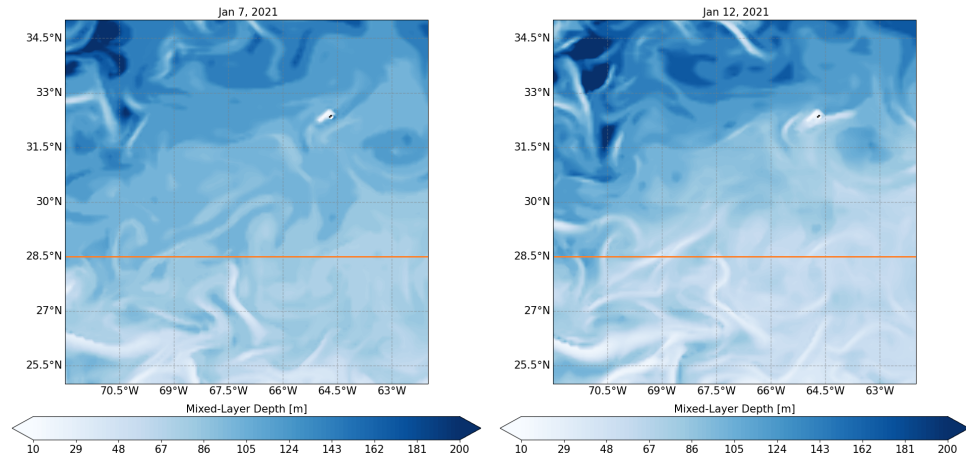
(A) Mixed-Layer Depth.



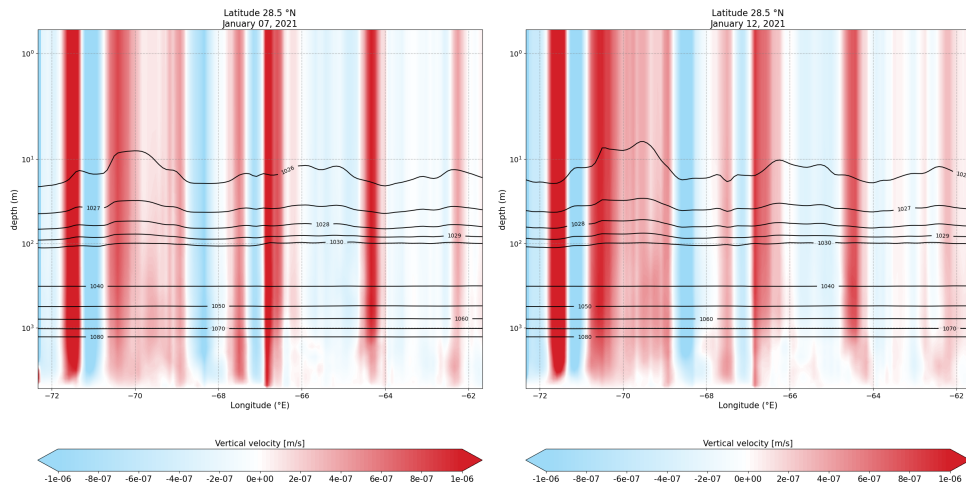
(B) Density and vertical velocities: zonal cross-section at 42 °N.

**FIGURE 3.6:** *Mixed-Layer Depth (a) and zonal transect of density and vertical velocities (b) in the Azores region: comparison between Jan 7 (left panels) and 12 (right panels), 2021. Zonal density profiles (black solid lines) are expressed in  $\text{kg}/\text{m}^3$ . The orange solid line shows the transect latitude.*

### 3.2. Vertical Insight



(A) Mixed-Layer Depth.



(B) Density and vertical velocities: zonal cross-section at 28.5 °N.

**FIGURE 3.7:** *Mixed-Layer Depth (a) and zonal transect of density and vertical velocities (b) in the Bermuda region: comparison between Jan 7 (left panels) and 12 (right panels), 2021. Zonal density profiles (black solid lines) are expressed in  $kg/m^3$ . The orange solid line shows the transect latitude.*

## Chapter 4

# Submesoscale Analysis in the Azores and Bermuda Regions

### Contents

---

<b>4.1 Parent-Child Comparison</b> . . . . .	<b>56</b>
4.1.1 Horizontal Features . . . . .	56
4.1.2 Vertical Insight and Mixed-Layer Instability . . . . .	65
<b>4.2 Submesoscale Structures from High-Resolution Fields</b> . . . . .	<b>76</b>

---

IN this chapter, we show the resulting fields from our high-resolution simulations and the results analysis. The aim is to study the onset of submesoscale processes in the two regions of interest, along with benefits of the high-resolution downscaled fields. We focus on January 7<sup>th</sup> and 12<sup>th</sup> 2021, i.e. the first simulation day after the spin-up period and the last one.

As seen in Chap. 3, the mesoscale analysis has pointed out the presence of restratification processes. Furthermore, Mixed-Layer Depth fluctuations during the simulation period would seem more connected to submesoscales than to mesoscales, i.e. they might reveal Mixed-Layer Instability. This would provide a link between mesoscale features and submesoscale activity. Through our high-resolution models, we aim to assess the role of Mixed-Layer Instability in the restratification process, as the coarser parent model does not seem to clearly reveal MLI occurrence.

In the following sections, we compare fields and vertical structures from the parent coarser simulation and the child high-resolution ones. In this context, relative vorticity, vertical velocities and vertical stratification are key variables for pointing out the benefits of the downscaling approach and detecting Mixed-Layer Instability. Lastly, we give few hints about submesoscale structures obtained from our high-resolution output fields.

### 4.1 Parent-Child Comparison

The benefits of the dynamical downscaling approach may appear when directly comparing resulting fields from both parent and child models. For this purpose, the high-resolution data obtained from the two child simulations have been daily averaged and interpolated on the parent computational grid. All the child fields shown within this section have been treated this way, except when otherwise specified. With the same approach as in Chap. 3, we firstly compare horizontal features, then vertical properties. In particular, we focus on horizontal current and vorticity fields nearly 10 m deep, vertical velocities and pycnoclines disposition. Furthermore, Kinetic Energy and Brunt-Väisälä frequency profiles are compared, yet decisive information is gained from the Rossby number distributions, too.

#### 4.1.1 Horizontal Features

In Figs 4.1 and 4.2, the current field comparisons at nearly 10 m depth are shown in both regions, on Jan 7 (Figs 4.1a and 4.2a) and Jan 12 (Figs 4.1b and 4.2b), 2021. However, they are just shown for sake of completeness as little information may be gained from this parent-child comparison. A part from small differences in speed intensity, there not seems to be significative structures detected only by child simulations. The child model reproduces very similar features to the ones discussed in Sec. 3.1.

An important impact of model resolution is the emergence in the relative vorticity field of smaller eddies and filamentary structures resulting from non-linear interactions. The relative vorticity  $\xi_z$  comparison is shown in Fig. 4.3 for the Azores and Fig. 4.4 for the Bermuda region. As visible, parent and child relative vorticity fields are very similar at the beginning, on Jan 7, 2021 (Figs 4.3a and 4.4a). This is comprehensible as the parent model feeds the

child one through initial and boundary conditions, thus they might be very similar during the first days. However, child model presents finer structures close to the various vortices, during the last simulation day. This is true especially in the north-eastern part of the Azores domain (Fig. 4.3b) and in the south-western part of the Bermuda one (Fig. 4.4b). These remarks are clearer when considering relative vorticity difference between parent and child models (Fig. 4.5). In both regions there are significative differences as the simulations progress. In fact, the child model seems to predict greater values than the parent ones along the whole Azores domain (Fig. 4.5a). This is true in the Bermuda region, too (Fig. 4.5b), with smaller effects around the domain center. Interestingly, the child model seems to clearly outline vorticity wakes in the leeward of the Bermuda island, which are not really distinguishable around the Azores where the vorticity field seems quite continuous.

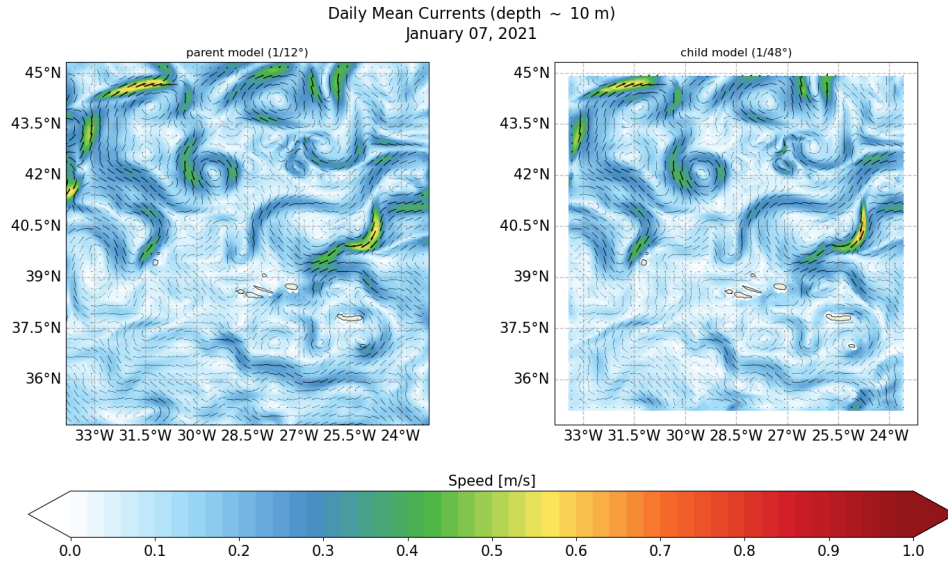
### Rosby Number Distribution

Going deeper into the high-resolution model benefits, the Rossby number  $R_o$  distributions are analysed in Fig. 4.6. Here, the daily mean  $R_o$  field is computed by dividing relative vorticity by the latitude-dependent Coriolis parameter  $f$ . Distributions are obtained considering the fields in Figs 4.3 and 4.4, so that they represent  $R_o$  occurrences at nearly 10 m depth. Their evolution is shown for both Azores (Fig. 4.6a) and Bermuda (Fig. 4.6b) regions. It can be seen that, starting from nearly overlapped shapes, parent and child distributions significantly deviate during the last simulation day, with the child ones reaching greater  $R_o$  absolute values. This is clearer comparing the distribution kurtosis and standard deviation values (Fig. 4.6c). In fact, the child distributions always tend to be wider than the parent ones, as the child standard deviation increases significantly more, in both regions. Child kurtosis are always far larger than the parent ones, so that the distribution tails are fatter. These aspects suggest the child model ability to better detect submesoscale currents identified by higher  $R_o$  values. Furthermore, while in the Azores region kurtosis decreases for both parent and child models, this is not true for the Bermuda one. Here, kurtosis significantly decreases for the parent while largely grows for the child. Thus, it might seem that submesoscale transition in our high-resolution simulations is appreciable in both regions. At lower latitudes, where the deformation radius is greater,

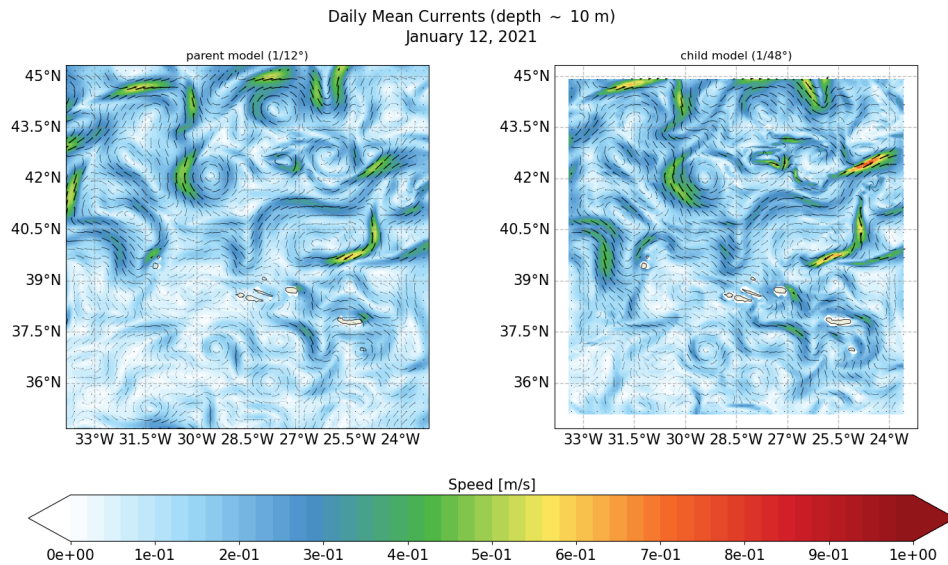
#### 4.1. Parent-Child Comparison

---

it would seem horizontal submesoscale currents are largely present, too, yet worse detected by the coarser global model. Differently, at higher latitudes the parent model seems to better predict the evolution of submesoscale currents, although underestimating their presence. In this sense, benefits of a dynamical downscaling approach would seem more appreciable at lower latitudes.



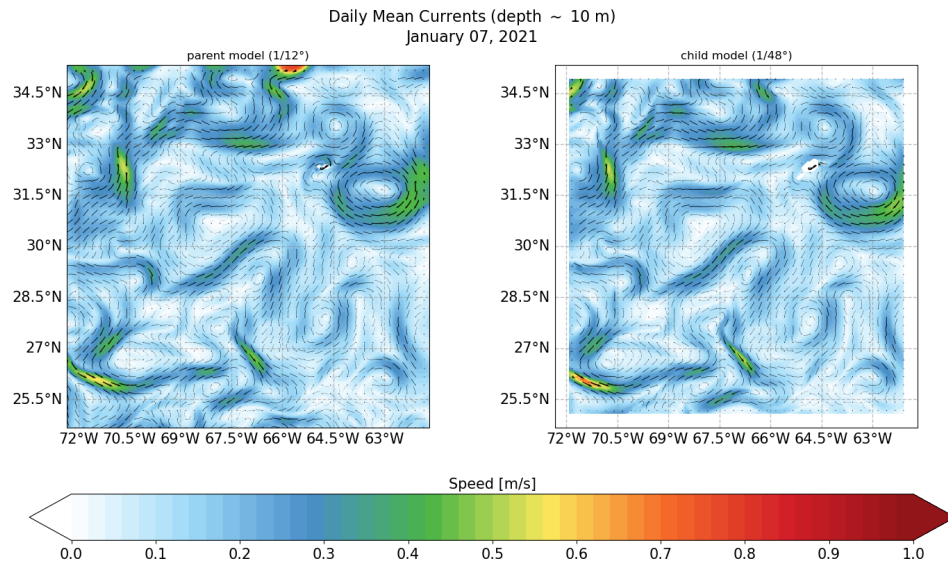
(A) 7 Jan, 2021.



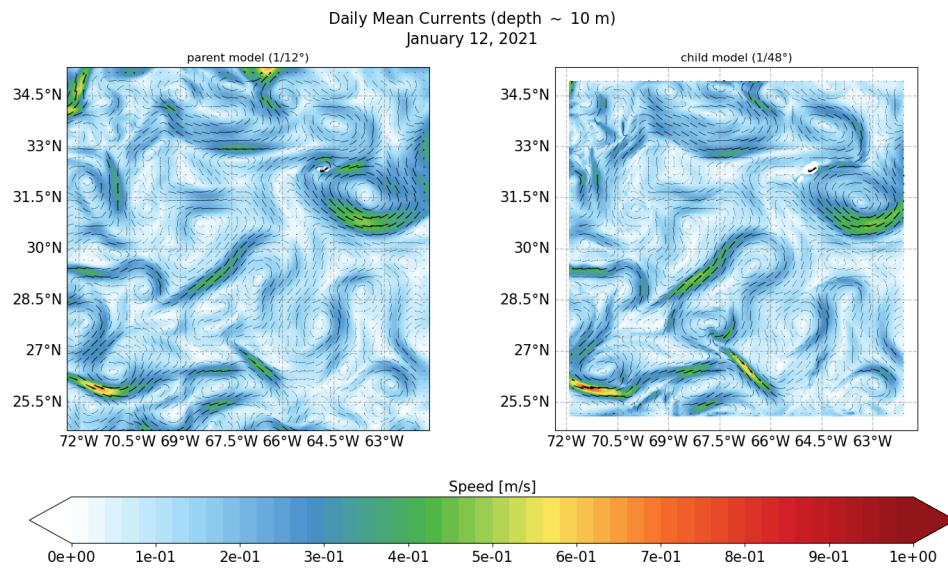
(B) 12 Jan, 2021.

**FIGURE 4.1:** Daily mean horizontal currents at nearly 10 m depth: comparison between parent and child models in the Azores region, on Jan 7 (a) and 12 (b), 2021.

#### 4.1. Parent-Child Comparison

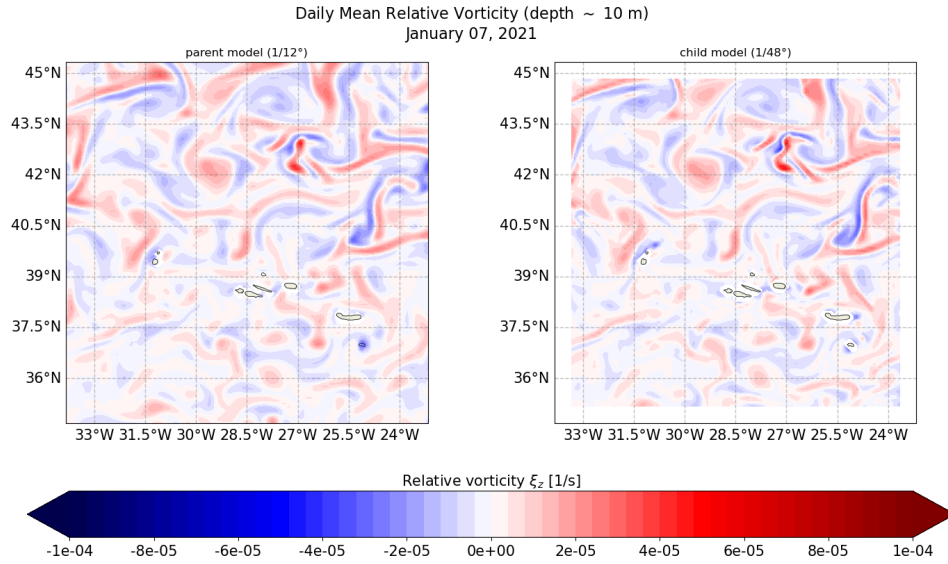


(A) 7 Jan, 2021.

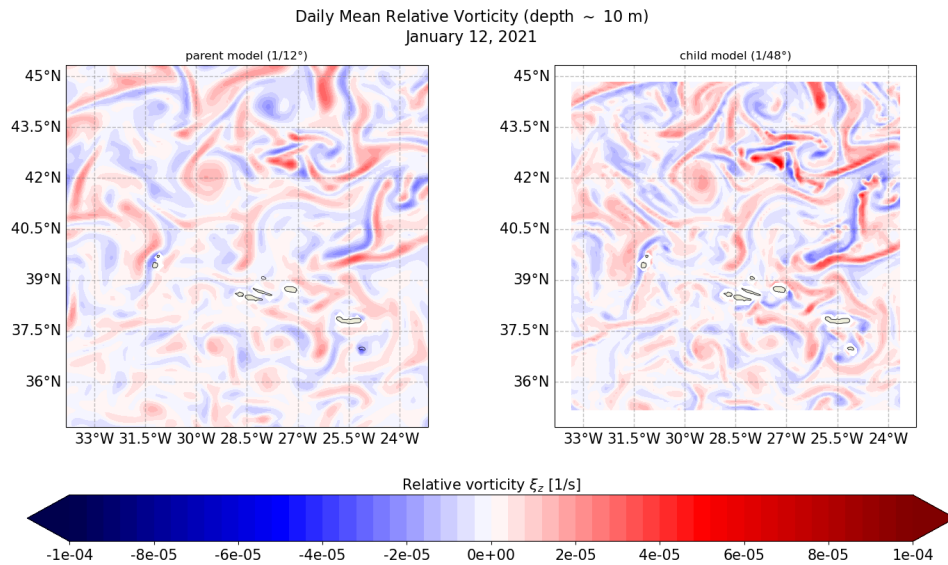


(B) 12 Jan, 2021.

**FIGURE 4.2:** Daily mean horizontal currents at nearly 10 m depth: comparison between parent and child models in the Bermuda region, on Jan 7 (a) and 12 (b), 2021.



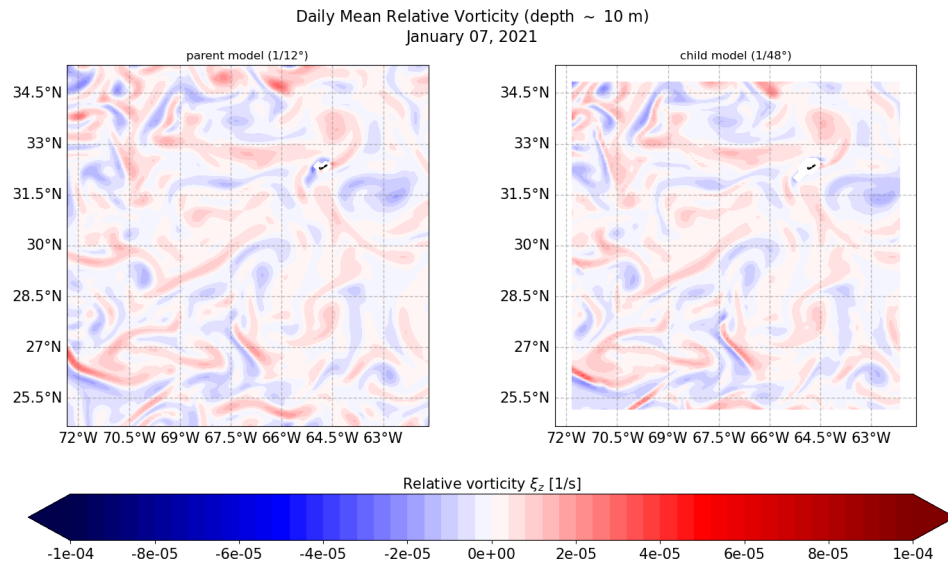
(A) 7 Jan, 2021.



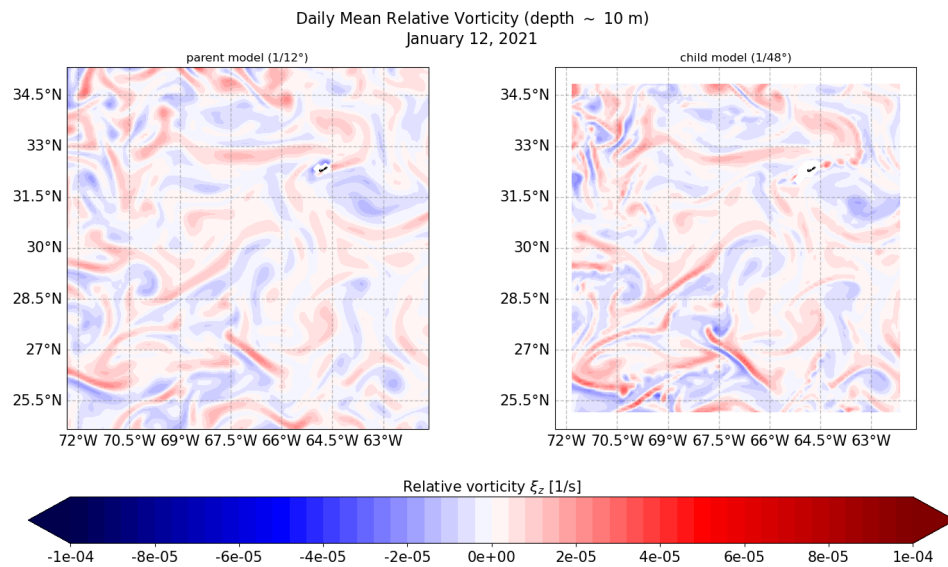
(B) 12 Jan, 2021.

**FIGURE 4.3:** Daily mean relative vorticity at nearly 10 m depth: comparison between parent and child models in the Azores region, on Jan 7 (a) and 12 (b), 2021.

## 4.1. Parent-Child Comparison

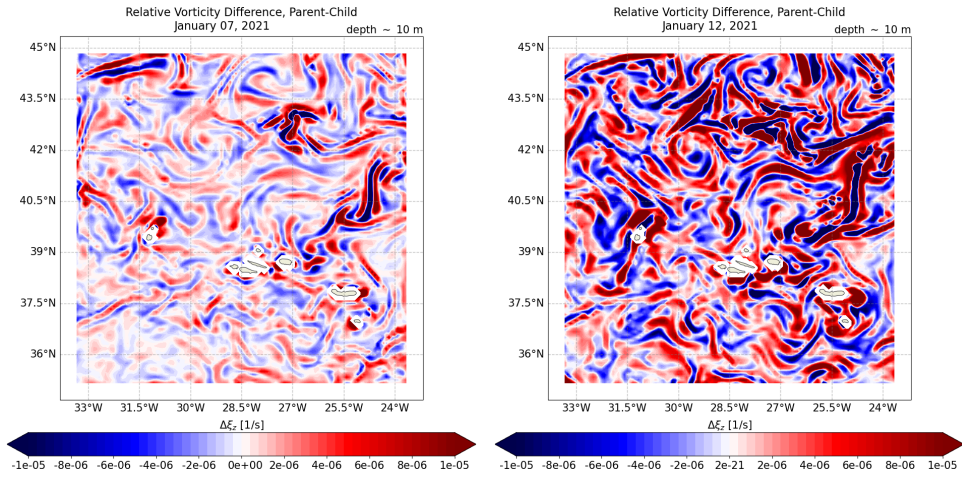


(A) 7 Jan, 2021.

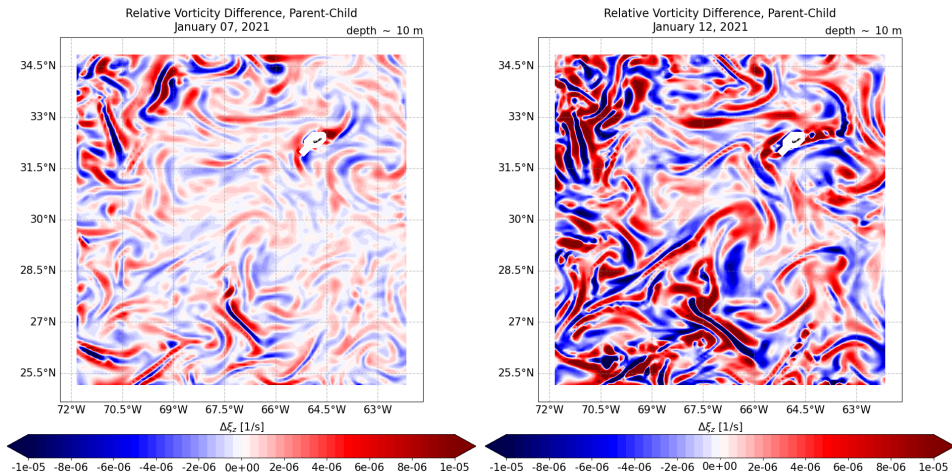


(B) 12 Jan, 2021.

**FIGURE 4.4:** Daily mean relative vorticity at nearly 10 m depth: comparison between parent and child models in the Bermuda region, on Jan 7 (a) and 12 (b), 2021.



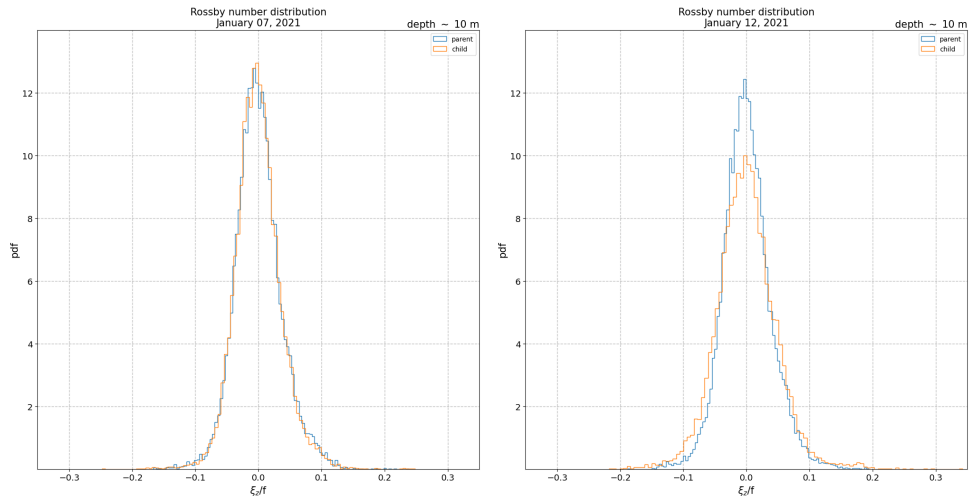
(A) Azores.



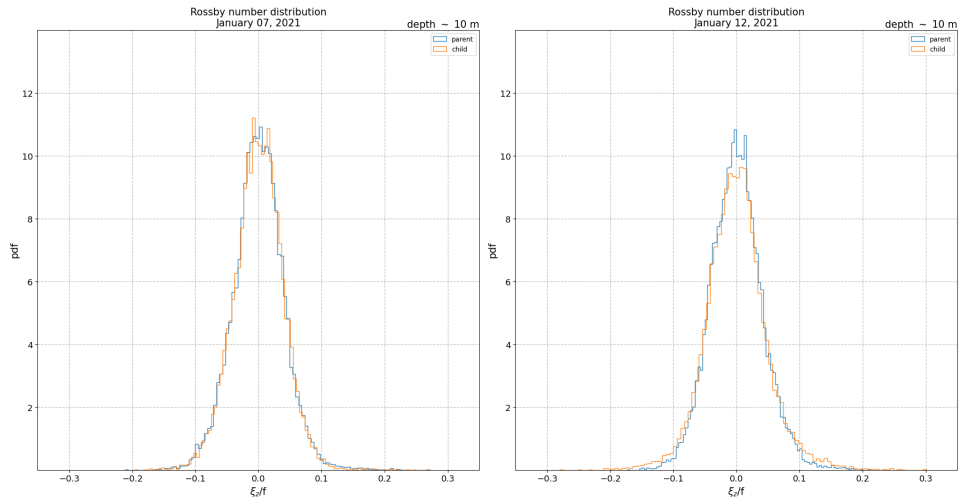
(B) Bermuda.

**FIGURE 4.5:** Daily mean relative vorticity difference between parent and child simulations, at nearly 10 m depth. The difference is shown in both Azores (a) and Bermuda (b) regions, on Jan 7 (left panels) and 12 (right panels), 2021.

## 4.1. Parent-Child Comparison



(A) Azores.



(B) Bermuda.

		Azores		Bermuda	
7 Jan, 2021		PARENT	CHILD	PARENT	CHILD
	kurtosis	1.30	2.34	1.26	1.50
	std dev.	0.037	0.037	0.040	0.040
12 Jan, 2021		PARENT	CHILD	PARENT	CHILD
	kurtosis	1.22	1.98	0.82	2.09
	std dev.	0.038	0.047	0.042	0.049

(C) Distributions' kurtosis and standard deviation.

**FIGURE 4.6:** Daily mean Rossby number distributions, computed from relative vorticity at nearly 10 m depth. Comparison between parent and child models in both Azores (a) and Bermuda (b) regions, on Jan 7 (left panels) and 12 (right panels), 2021. In (c), a table for comparing the distributions' kurtosis and standard deviation.

### 4.1.2 Vertical Insight and Mixed-Layer Instability

We now proceed with an insight of the vertical properties, which may be determinant to assess if Mixed-Layer Instability (MLI) really occurs, as hinted by the mesoscale analysis.

We start from the daily mean Mixed-Layer Depth (MLD) comparisons (Figs 4.7 and 4.8). The MLD field seems to be very similar between parent and child models, during both Jan 7 (Figs 4.7a, 4.8a) and Jan 12 (Figs 4.7b, 4.8b). The parent MLD excursions are confirmed by the child, though the high-resolution model reproduces finer and more detailed structures in the MLD field. Furthermore, the MLD fluctuations of order  $O(\text{days})$ , pointed out in Sec. 3.2, may be found in the child results, too. In Fig. 4.9, the temporal evolution of the daily MLD averaged over the entire area is shown for both parent and child models during the simulation period, in both regions. As it appears, they are quite similar, though the child model predicts a slightly different trend.

#### Vertical Velocities

From the parent-child comparison of MLD fluctuations, it would seem MLI may occur during the simulation days, in both regions. However, the parent model alone has not been sufficient to determine the effective presence of MLI, as the parent vertical velocities remains quite constant during the simulation (see Sec. 3.2). On the contrary, here child vertical velocities seem to be completely different than the parent ones, as visible in Figs 4.10 and 4.11 where the zonal cross-sections are compared between parent and child, respectively in the Azores and Bermuda regions. Child vertical velocity values are of order  $O(10^{-5} \div 10^{-6})$ , i.e. one order of magnitude greater than the parent ones. Furthermore, child fields present a reachness of structures not achieved by the parent one, even during the first simulation day (Figs 4.10a and 4.11a). Vertical velocities variability is very significative, as the fields present great differences during the last simulation day (Figs 4.10b and 4.11b). To notice, vertical velocities far increase near the surface during Jan 12, 2021 in the Azores, while decrease in the Bermuda case. This may be partly related to the nearly surfacing of the MLD in a consistent part of the Azores region. However, vertical velocities significantly vary in both

regions, especially along the first hundred meters depth.

### Mixed-Layer Instability and Restratification

From vertical velocities comparison, it would really seem child model is able to detect MLI in both regions, unlike the parent. To assess its effectiveness in the restratification process, we now focus on the first hundreds meters in both regions. For this purpose, in Fig. 4.12 we show the same cross-section, where parent and child density profiles and MLD are compared during the last simulation day. Furthermore, the child vertical velocity field is shown in the background.

As it appears, the child model pycnoclines are smoother than the parent ones in the Azores region (Fig. 4.12a). Here, we may see child simulation predicts lower density gradients within the first hundred meters, i.e. the restratification process seems to be towards the end. Differently, in the Bermuda domain (Fig. 4.12b) density gradients are still strong, being far from the end of the restratification process. If we consider MLD and pycnoclines disposition along the two transects, we notice consistent differences between the two regions. While in the Azores one we have big spatial fluctuations of the MLD and nearly-horizontal pycnoclines, in the Bermuda region MLD and pycnoclines have similar trends. Thus, it might seem that pycnoclines simply oscillates as the MLD does in the Bermuda region, while in the Azores the greater MLD oscillations would coexist with restratification. Through child model, these behaviours are emphasized with respect to the parent one, as the MLD shape becomes even closer to the pycnoclines one in the Bermuda, while MLD spatial variability increases even more in the Azores. This may induce us to think MLI occurs in the Azores region and plays a role in the restratification process, though it does not seem to significantly contribute to restratification in the Bermuda one, where MLD fluctuations are smaller. Thus, it would be important to assess if MLI actually occurs in the Bermuda domain, to determine its role related to the deformation radius.

To assess the presence of MLI in both regions, we now analyse the Kinetic Energy (KE) and Brunt-Vaisala (BV) frequency profiles (Fig. 4.13). The KE profile is computed averaging the horizontal velocities over each depth layer, as

$$\langle KE(z) \rangle = \frac{1}{\Delta x \Delta y} \int_{\Delta x} \int_{\Delta y} (u^2(z) + v^2(z)) dx dy \quad .$$

The two profiles are obtained over a limited area of interest, where great MLD variability occurs, i.e.  $40.5 \div 43.5^\circ\text{N} \times 25.5 \div 31.5^\circ\text{W}$  for the Azores,  $27 \div 30^\circ\text{N} \times 63 \div 69^\circ\text{W}$  for the Bermuda case. As visible, child model provides a smoother BV frequency profile with soften peaks, both in the Azores and Bermuda (Figs 4.13a and 4.13b, left panels). This confirms the idea that restratification processes are taking place, as already suggested by the mesoscale analysis. Furthermore, from the KE vertical profiles (Figs 4.13a and 4.13b, right panels), we see that child model detects higher KE values along the first hundreds meter depth. This is particularly true for the Azores region, where a large piece of KE seems to be trapped within the surface layer, coherently with MLI theory. Here, MLI allows the conversion from potential energy to kinetic one, producing horizontal and vertical ageostrophic (submesoscale) currents contributing to restratification. The KE structure is not similarly net in the Bermuda area, though the difference between parent and child is appreciable. This might lead to say MLI is present here, too, generating submesoscale horizontal and vertical currents as the ones shown through the previous velocity fields analysis. Still, it would not be determinant in restratifying the Bermuda area. Hopefully, future double nestings in this region might lead to a KE profile more similar to the one obtained in the Azores. If we compare our results with the one obtained by [Beaudin et al. \(2019\)](#) who carries out a double nesting in the Caribbean Sea, this might seem the right approach.

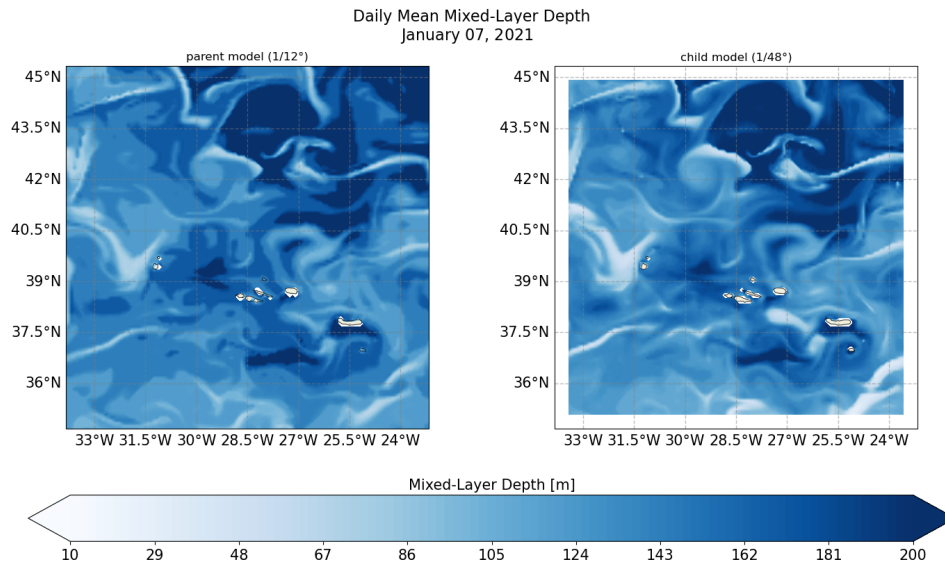
To note at last, the KE profiles in Fig. 4.13 may reveal frontogenesis which is linked to the same potential-to-kinetic energy conversion as MLI. Thus, frontogenesis might contribute to submesoscale currents generation in both regions.

In conclusion, it would seem that our high-resolution downscaled fields reveal the presence of MLI instability in both regions, which contributes to the generation of horizontal and vertical submesoscale currents. Furthermore, MLI seems to play a key role among restratification processes in the Azores region, while its effectiveness could be excluded in restratifying the Bermuda one. This might be coherent with the baroclinic deformation radius of the two regions: as in the Bermuda it assumes higher values, the restratification processes would occur at larger scales than the submesoscales, so that

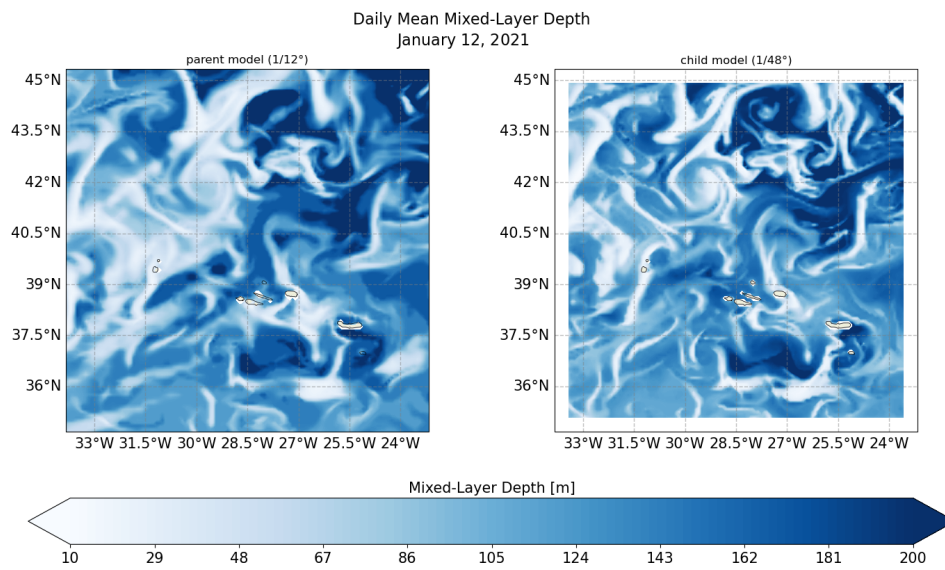
#### 4.1. Parent-Child Comparison

---

MLI is not determinant in restratifying the water column. Higher-resolution simulations might further assess the presence of MLI in the Bermuda region, confirming this is not a dominant restratification process at lower latitude where the deformation radius is larger.



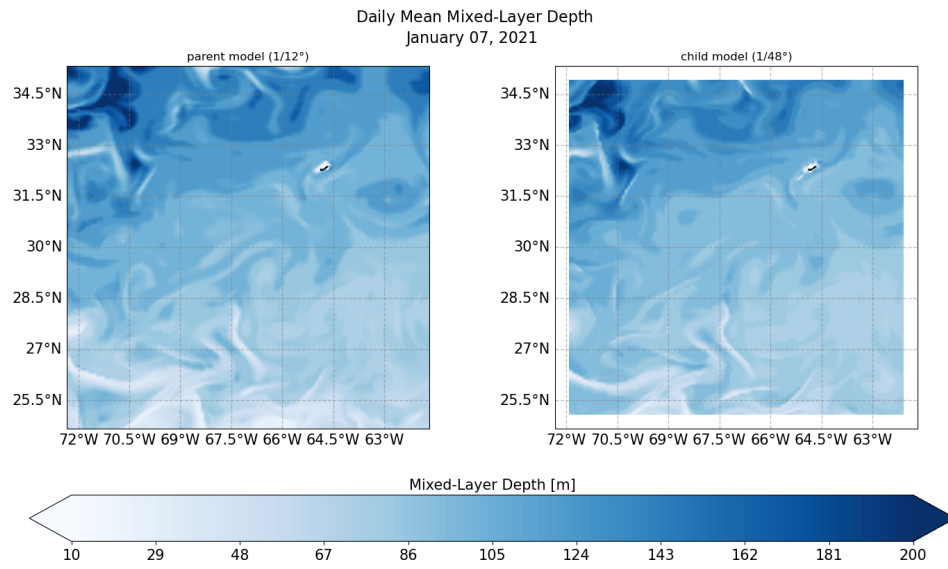
(A) 7 Jan, 2021.



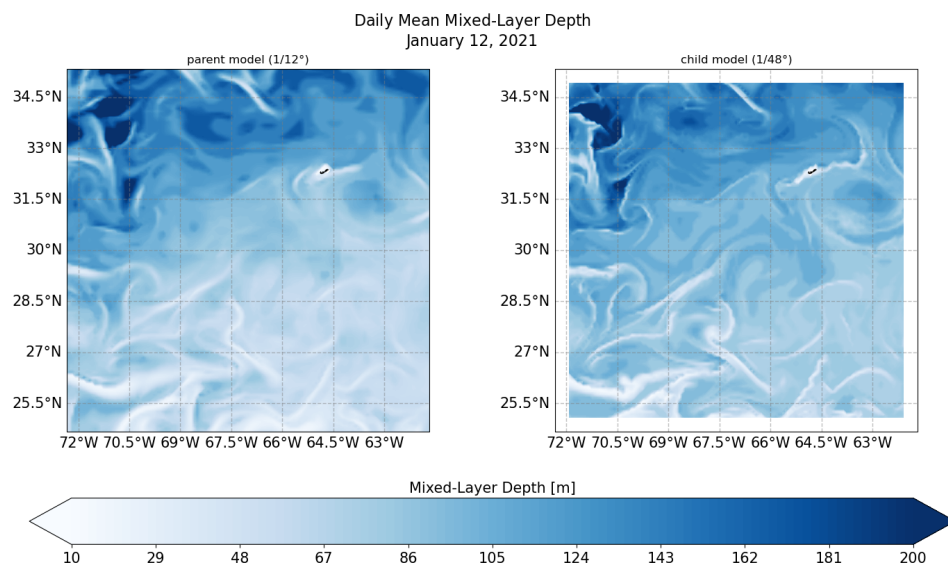
(B) 12 Jan, 2021.

**FIGURE 4.7:** Daily mean Mixed-Layer Depth: comparison between parent and child models in the Azores region, on Jan 7 (a) and 12 (b), 2021.

#### 4.1. Parent-Child Comparison



(A) 7 Jan, 2021.



(B) 12 Jan, 2021.

**FIGURE 4.8:** Daily mean Mixed-Layer Depth: comparison between parent and child models in the Bermuda region, on Jan 7 (a) and 12 (b), 2021.

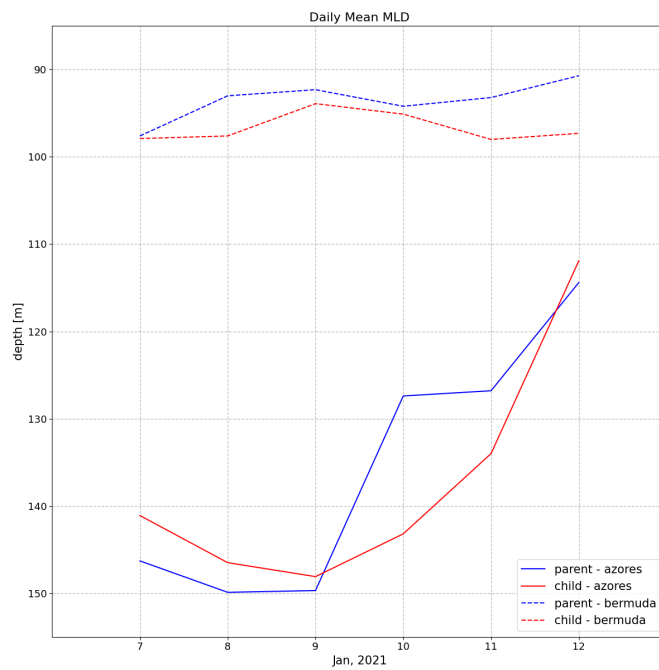
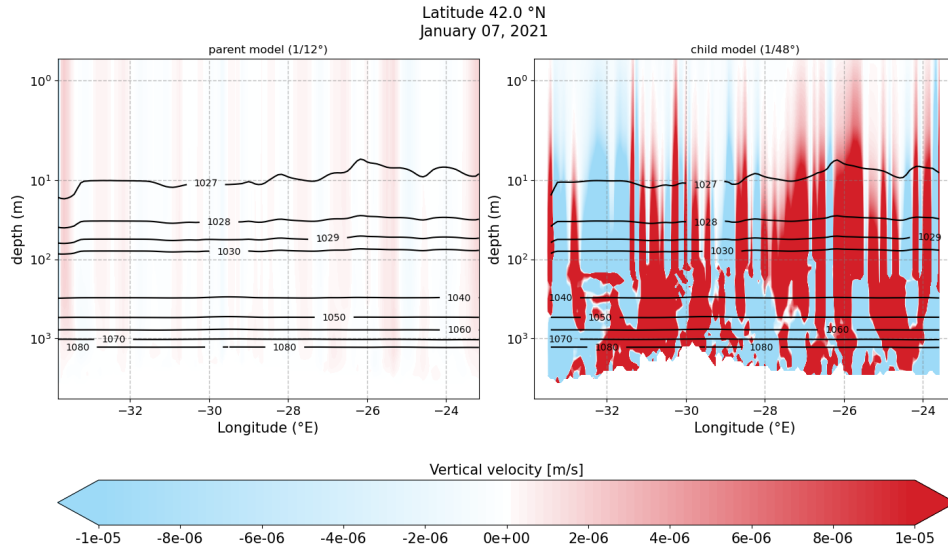
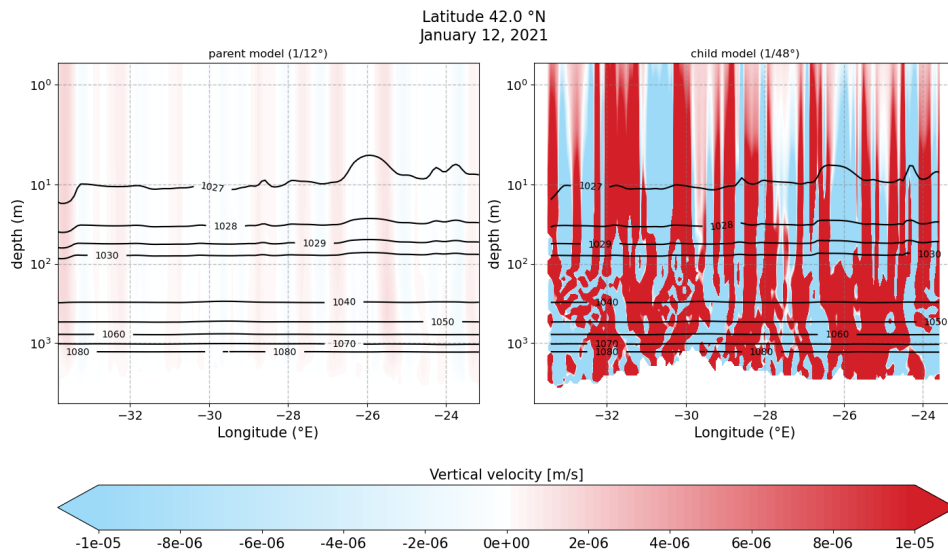


**FIGURE 4.9:** *Mixed-Layer Depth evolution during the simulation period: comparison between parent and child models in both Azores (solid lines) and Bermuda (dashed lines) regions.*

#### 4.1. Parent-Child Comparison

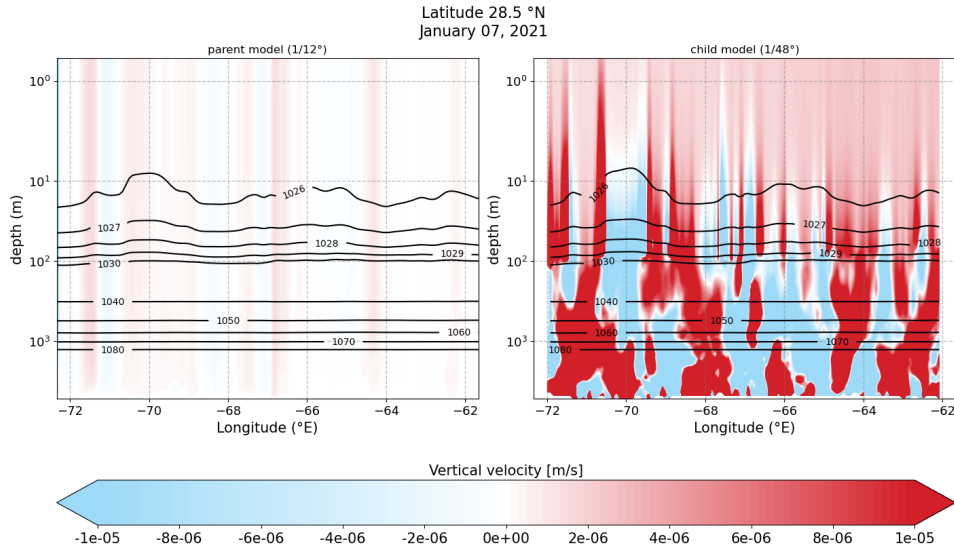


(A) 7 Jan, 2021.

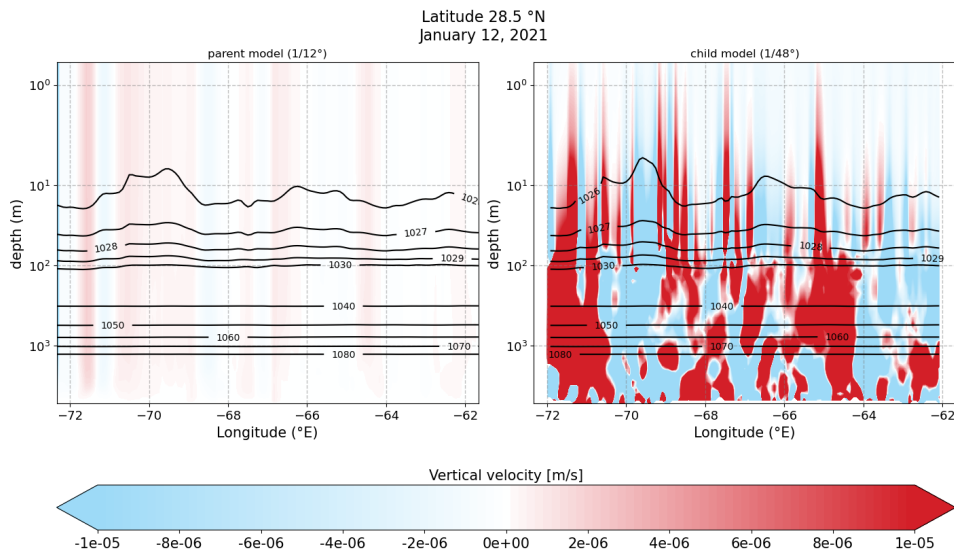


(B) 12 Jan, 2021.

**FIGURE 4.10:** Zonal transect of density and vertical velocities at 42 °N in the Azores region: comparison between parent and child models, on Jan 7 (a) and 12 (b), 2021. Zonal density profiles (black solid lines) are expressed in  $\text{kg/m}^3$ .



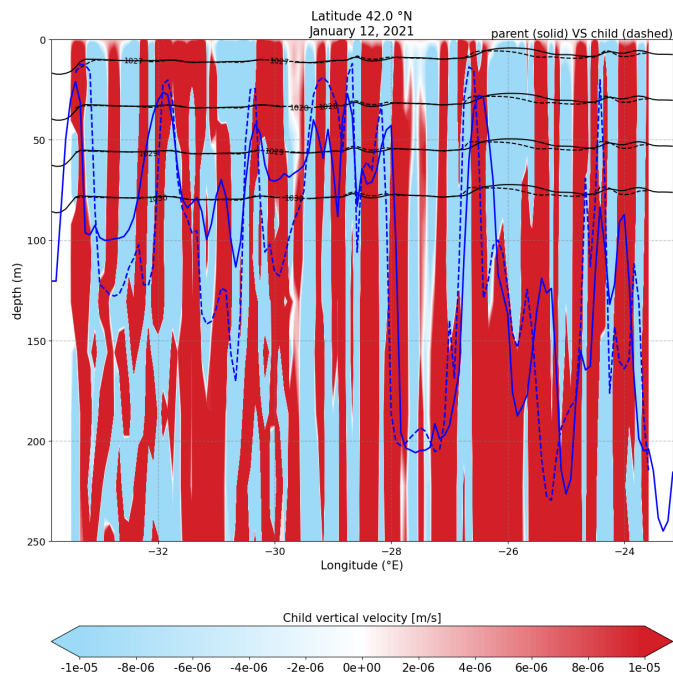
(A) 7 Jan, 2021.



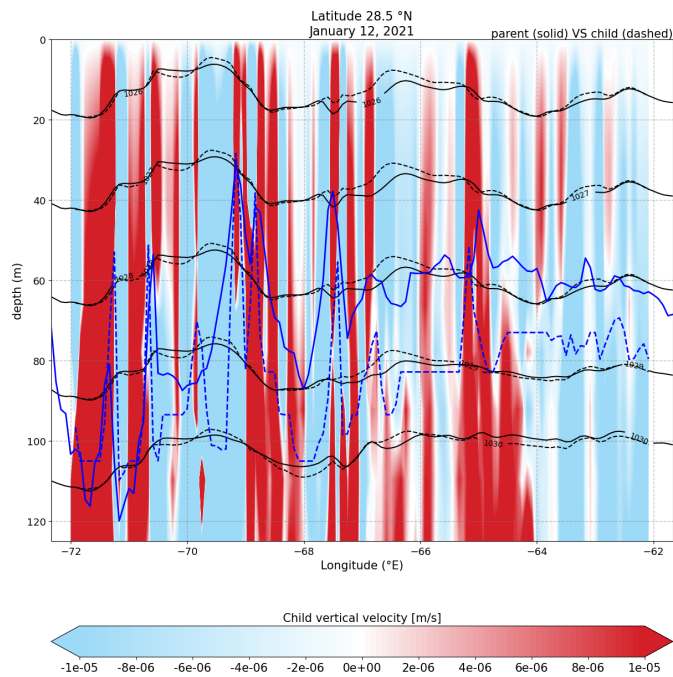
(B) 12 Jan, 2021.

**FIGURE 4.11:** Zonal transect of density and vertical velocities at 28.5 °N in the Bermuda region: comparison between parent and child models, on Jan 7 (a) and 12 (b), 2021. Zonal density profiles are expressed in  $\text{kg}/\text{m}^3$ .

#### 4.1. Parent-Child Comparison

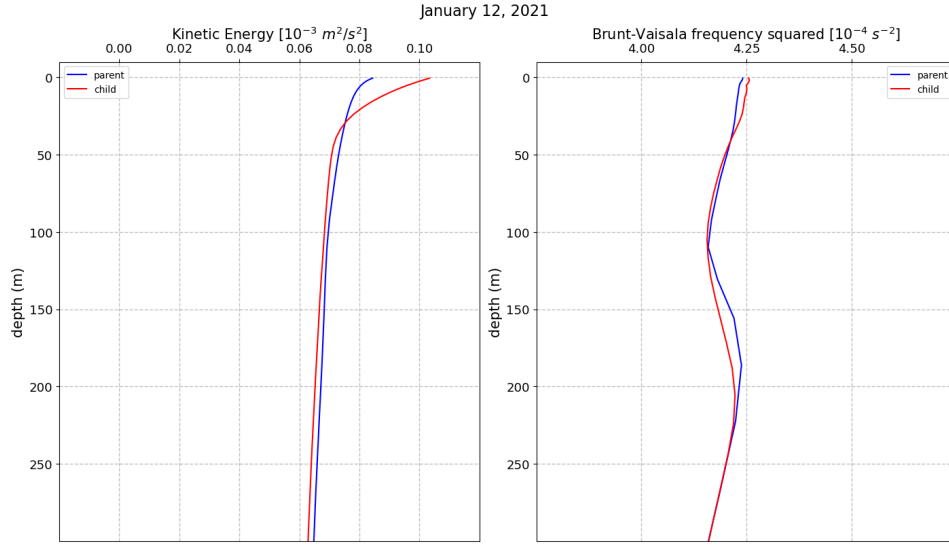


(A) Azores.

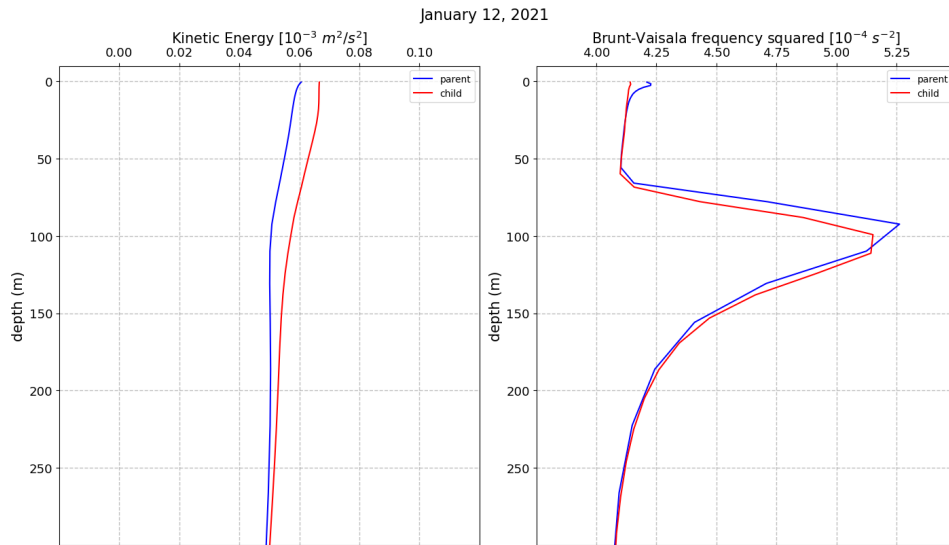


(B) Bermuda.

**FIGURE 4.12:** Zonal transects of density (black lines) and MLD (blue lines), with focus on the first hundreds meters, at  $42^\circ N$  in the Azores (a) and  $28.5^\circ N$  in the Bermuda region (b). The comparison between parent (solid lines) and child (dashed lines) models is shown on Jan 12, 2021. Zonal density profiles are expressed in  $\text{kg/m}^3$ . The child vertical velocities are shown (coloured field).



(A) Azores.



(B) Bermuda.

**FIGURE 4.13:** Profiles of daily mean Kinetic Energy (left panels) and Brunt-Vaisala frequency squared (right panels), on Jan 12, 2021. Comparison between parent and child models in both Azores (a) and Bermuda (b) regions. The mean vertical profiles are computed over an area of interest:  $40.5 \div 43.5^\circ \text{N} \times 25.5 \div 31.5^\circ \text{W}$  for the Azores,  $27 \div 30^\circ \text{N} \times 63 \div 69^\circ \text{W}$  for the Bermuda case.

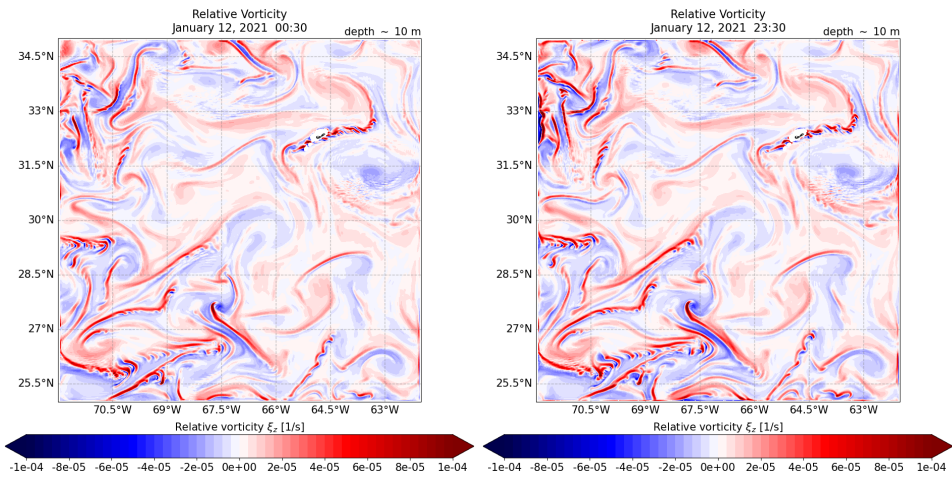
## 4.2 Submesoscale Structures from High-Resolution Fields

Few last considerations might regard submesoscale structures showing up from our high-resolution fields. In particular, relative vorticity and temperature seems to be useful variables for studying horizontal structures.

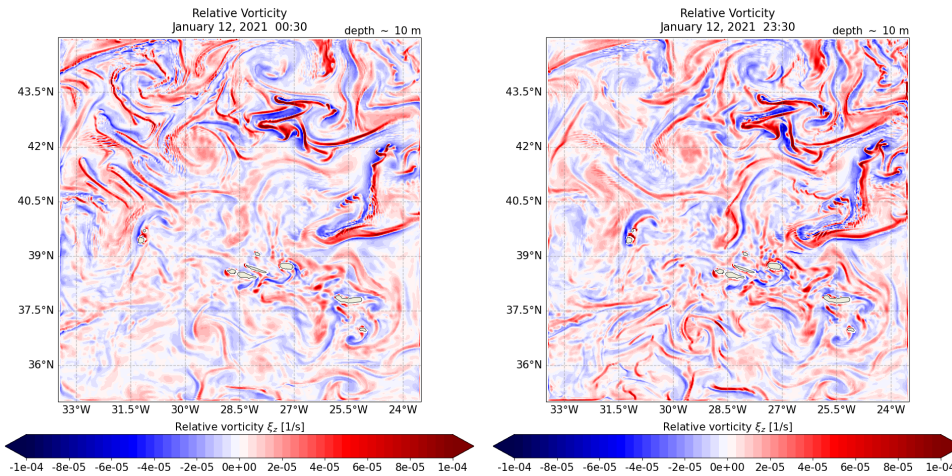
We show hourly vorticity and temperature fields evolution on Jan 12, 2021 in both regions (Fig.s 4.14 and 4.15). The hourly fields are shown at 0:30 and 23:30, to observe both persistent and varying structures. As it appears, the dynamical downscaling approach really allows to appreciate the submesoscale structures richness. Vortices and thin filaments evolve along the whole domain. In addition, clear fronts may be noticed (Fig.s 4.15b and 4.15a). Thus, frontogenesis seems to take place, probably contributing to submesoscale currents generation as hinted by the previously discussed KE profiles (Fig. 4.13, left panels).

Besides, in the Bermuda region (Fig. 4.14a) it immediately appears the Bermuda island generates clear leeward vorticity wakes. In the Azores region (Fig. 4.14b), this similarly happens around the solitary Flores island (the north-western one). Where the other islands are compact, vorticity field results to be very crumbled. These vorticity perturbations are known for their contribute to submesoscale currents generation, too, as shown by theory and previous studies.

All things considered, we might say MLI is only one of the processes contributing to submesoscale currents generation, in the regions of interest. In fact, it seems other mechanisms are active, such as frontogenesis and topographic wakes. Therefore, the dynamical downscaling approach allows us to detect submesoscale activity generated through various ways (MLI, frontogenesis and topographic wakes). While in the Bermuda region MLI appears to be simply one among them, in the Azores it seems determinant for restratification, too.



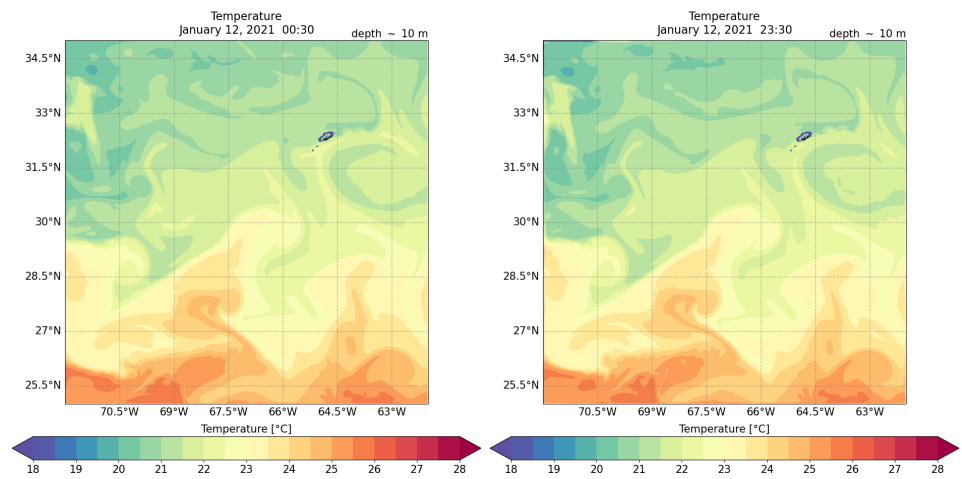
(A) Bermuda.



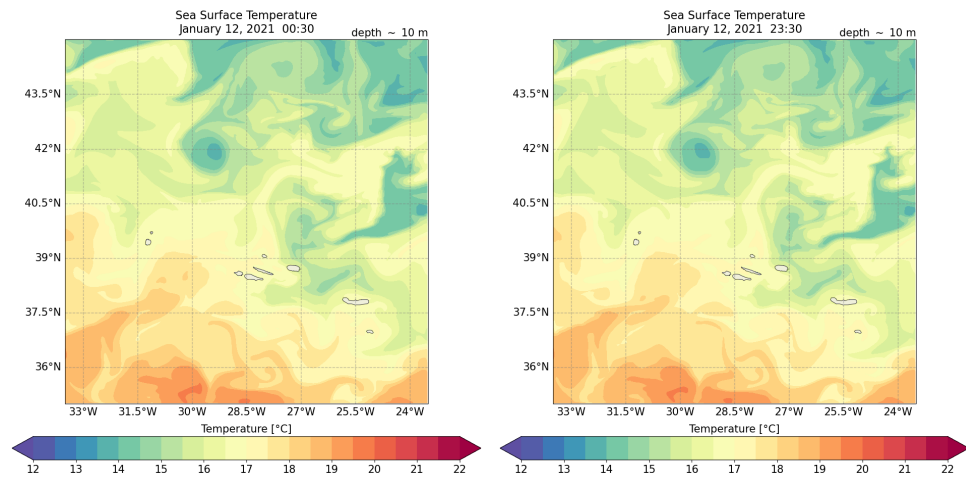
(B) Azores.

**FIGURE 4.14:** Hourly relative vorticity at nearly 10 m depth, obtained from child simulations in the Bermuda (a) and Azores (b) regions. The fields are shown at 0:30 (left panels) and 23:30 (right panels), on Jan 12, 2021.

## 4.2. Submesoscale Structures from High-Resolution Fields



(A) Bermuda.



(B) Azores.

**FIGURE 4.15:** Hourly temperature field at nearly 10 m depth, obtained from child simulations in the Bermuda (a) and Azores (b) regions. The fields are shown at 0:30 (left panels) and 23:30 (right panels), on Jan 12, 2021.

# Chapter 5

## Conclusion

This study has investigated the onset of submesoscale activity and its relation with the baroclinic deformation radius, in two regions of the North Atlantic Ocean. Through the NEMO-based SURF platform (Structured and Unstructured grid Relocatable ocean platform for Forecasting), a dynamical downscaling approach allows to carry out two nested high-resolution simulations at  $1/48^\circ$  resolution, called "child". These are obtained starting from a global ocean general circulation model at  $1/12^\circ$  resolution, called "parent", provided by the Copernicus Marine Environment Monitoring Service (CMEMS). The simulation time-period goes from January 4<sup>th</sup> to 12<sup>th</sup>, 2021. The first three days are treated as spin-up period.

From a first mesoscale analysis based on parent global model information, it seems the main horizontal mesoscale eddies persist during the simulation days, in both regions. In particular, in the Bermuda region eddies are wider as the baroclinic deformation radius assumes larger values at these latitudes. Studying the Brunt-Väisälä frequency vertical profile, it appears restratification processes take place during the simulation period. Furthermore, the Mixed-Layer Depth (MLD) field presents  $O(\text{days})$  variability, with small excursions in the Bermuda region while far larger amplitudes in the Azores. This may be a key revealing the presence of Mixed-Layer Instability (MLI), which would provide a connection between mesoscales and submesoscales. However, MLI is typically related to large vertical velocity structures quickly changing, which are not detected by the parent model.

A submesoscale analysis follows, based on the comparison between parent and child resulting daily mean fields. An important impact of model reso-

---

lution reveals to be the emergence in the relative vorticity field of smaller eddies and filamentary structures. Comparing the Rossby number distribution obtained from both parent and child vorticity fields, it results the child distributions are wider, characterized by larger values of standard deviation and kurtosis. This means the dynamical downscaling approach reveals submesoscale horizontal currents which are not detected by the coarser parent model. Besides, parent ability to detect submesoscale currents seems to get worse at lower latitude where submesoscale activity is still intense. From a vertical insight, the  $O(\text{days})$  MLD oscillations from the mesoscale analysis are confirmed by child simulations, along with the restratification tendency. Nevertheless, the high-resolution fields show much greater vertical velocities which vary from one day to another. This allows the detection of MLI in both regions, as confirmed by Kinetic Energy (KE) profiles. In fact, the child model predicts significantly higher KE values in the surface layer, with a net profile in the Azores region. However, while in the Azores MLI seems to be determinant in the restratification process, in the Bermuda region it seems restratification takes place at mesoscales rather than submesoscales. The greater eddies length-scale seems to influence the vertical structure at longer time scales, so that MLI is not effective in restratifying the water column. Lastly, the analysis of high-resolution fields allows to notice fronts, filaments and topographic wakes, coherently with the surface-intensified KE profiles obtained in the two regions of interest. Thus, MLI would be one of the processes generating submesoscale currents in both regions.

In conclusion, our dynamical downscaling approach allows the detection of submesoscale activity in both regions, in the form of horizontal and vertical submesoscale currents generated by MLI, frontogenesis and topographic wakes. These processes seem to activate beyond the baroclinic deformation radius value. However, the deformation radius might determine MLI role among the restratification processes. At lower latitudes where it assumes larger values, mesoscale eddies affects the density field at longer time scales. Thus, MLI does not seem effective in the restratification process which would occur at mesoscales, instead. In this sense, MLI would provide a connection between mesoscales and submesoscales.

# Bibliography

- Ajayi, A., J. Le Sommer, E. Chassignet, J.M. Molines, X. Xu, A. Albert, and E. Cosme (2020). “Spatial and temporal variability of the North Atlantic eddy field from two kilometeric-resolution ocean models”. In: *Journal of Geophysical Research: Oceans* 125, e2019JC015827. DOI: [10.1029/2019JC015827](https://doi.org/10.1029/2019JC015827) (cit. on pp. 21, 38).
- Beaudin, Elise, Arne Biastoch, and Nadia Pinardi (2019). “Mesoscale and submesoscale dynamics in the Caribbean Sea”. Master thesis. CHRISTIAN-ALBRECHTS-UNIVERSITÄT ZU KIEL. URL: [https://www.sincem.unibo.it/images/tesi/tesi\\_master\\_beaudin.pdf](https://www.sincem.unibo.it/images/tesi/tesi_master_beaudin.pdf) (cit. on p. 67).
- Becker, J., David Sandwell, Walter Smith, et al. (2009). “Global bathymetry and elevation data at 30 arc seconds resolution: SRTM30 PLUS”. In: *Marine Geodesy*. DOI: [10.1080/01490410903297766](https://doi.org/10.1080/01490410903297766) (cit. on p. 39).
- Boccaletti, Giulio, Raffaele Ferrari, and Baylor Fox-Kemper (2007). “Mixed Layer Instabilities and Restratification”. In: *Journal of Physical Oceanography* 37.9, pp. 2228 –2250. DOI: [10.1175/JP03101.1](https://doi.org/10.1175/JP03101.1) (cit. on p. 50).
- Cao, Haijin, Baylor Fox-Kemper, and Zhiyou Jing (2021). “Submesoscale Eddies in the Upper Ocean of the Kuroshio Extension from High-Resolution Simulation: Energy Budget”. In: *Journal of Physical Oceanography* 51.7, pp. 2181 –2201. DOI: [10.1175/JP0-D-20-0267.1](https://doi.org/10.1175/JP0-D-20-0267.1) (cit. on p. 23).
- Chapron, B., V. Kudryavtsev, F. Collard, Nicolas Rasche, A. Kubryakov, and Sergey Stanichny (Dec. 2020). “Studies of Sub-Mesoscale Variability of the Ocean Upper Layer Based on Satellite Observations Data”. In: *Physical Oceanography* 27. DOI: [10.22449/1573-160X-2020-6-619-630](https://doi.org/10.22449/1573-160X-2020-6-619-630) (cit. on p. 20).
- Cheng, Yu-Hsin, Ming-Huei Chang, Dong S. Ko, Sen Jan, Magdalena Andres, Anthony Kirincich, Yiing Jang Yang, and Jen-Hua Tai (2020). “Submesoscale Eddy and Frontal Instabilities in the Kuroshio Interacting With

- a Cape South of Taiwan”. In: *Journal of Geophysical Research: Oceans* 125.5. DOI: [10.1029/2020JC016123](https://doi.org/10.1029/2020JC016123) (cit. on p. 23).
- Chune, S. Law, L. Nouel, E. Fernandez, Corinne Derval, M.Tressol, and R. Dussurget (2021). *PRODUCT USER MANUAL For the GLOBAL Ocean Sea Physical Analysis and Forecasting Products*. Issue: 1.8. Copernicus marine service. URL: <https://catalogue.marine.copernicus.eu/documents/PUM/CMEMS-GLO-PUM-001-024.pdf> (cit. on pp. 39, 50).
- Climate Modelling Center (2022). *NEMO ocean engine*. Scientific Notes of Climate Modelling Center, 27. ISSN: 1288-1619. Institut Pierre-Simon Laplace (IPSL). DOI: [10.5281/zenodo.1464816](https://doi.org/10.5281/zenodo.1464816) (cit. on p. 34).
- Dominicis, M. De, S. Falchetti, F. Trotta, N. Pinardi, et al. (2014). “A relocatable ocean model in support of environmental emergencies”. In: *Ocean Dynamics* 64.5, pp. 667–688. DOI: [10.1007/s10236-014-0705-x](https://doi.org/10.1007/s10236-014-0705-x) (cit. on p. 34).
- Egbert, Gary D., Andrew F. Bennett, and Michael G. G. Foreman (1994). “TOPEX/POSEIDON tides estimated using a global inverse model”. In: *Journal of Geophysical Research: Oceans* 99.C12, pp. 24821–24852. DOI: [10.1029/94JC01894](https://doi.org/10.1029/94JC01894) (cit. on p. 41).
- Egbert, Gary D. and Svetlana Y. Erofeeva (2002). “Efficient Inverse Modeling of Barotropic Ocean Tides”. In: *Journal of Atmospheric and Oceanic Technology* 19.2, pp. 183–204. DOI: [10.1175/1520-0426\(2002\)019<0183:EIMOB0>2.0.CO;2](https://doi.org/10.1175/1520-0426(2002)019<0183:EIMOB0>2.0.CO;2) (cit. on p. 41).
- Essink, S., V. Hormann, L.R. Centurioni, and A. Mahadevan (2019). “Can We Detect Submesoscale Motions in Drifter Pair Dispersion?” In: *Journal of Physical Oceanography* 49(9), 2237-2254. DOI: [10.1175/JPO-D-18-0181.1](https://doi.org/10.1175/JPO-D-18-0181.1) (cit. on p. 20).
- Fofonoff, N. and R. Millard (1983). “Algorithms for Computation of Fundamental Properties of Seawater”. In: *UNESCO Tech. Pap. Mar. Sci.* 44. DOI: [10.25607/OBP-1450](https://doi.org/10.25607/OBP-1450) (cit. on p. 49).
- Grilli, Federica and Nadia Pinardi (1999). *Le Cause Dinamiche della Stratificazione Verticale nel Mediterraneo*. technical report 3. ISAO, CNR (cit. on pp. 25–27).
- Gula, Jonathan, Tanya M. Blacic, and Robert E. Todd (2019). “Submesoscale Coherent Vortices in the Gulf Stream”. In: *Geophysical Research Letters* 46.5, pp. 2704–2714. DOI: [10.1029/2019GL081919](https://doi.org/10.1029/2019GL081919) (cit. on p. 23).

- Gula, Jonathan, M. Jeroen Molemaker, and James C. McWilliams (2016). “Submesoscale Dynamics of a Gulf Stream Frontal Eddy in the South Atlantic Bight”. In: *Journal of Physical Oceanography* 46.1, pp. 305 – 325. DOI: [10.1175/JPO-D-14-0258.1](https://doi.org/10.1175/JPO-D-14-0258.1) (cit. on p. 23).
- Haine, T. W. N., R. Gelderloos, M. A. Jimenez-Urias, A. Siddiqui, et al. (2021). “Is Computational Oceanography Coming of Age?” In: *Bulletin of the American Meteorological Society* 102(8), E1481-E1493. DOI: [10.1175/BAMS-D-20-0258.1](https://doi.org/10.1175/BAMS-D-20-0258.1) (cit. on p. 20).
- LaCasce, J. H. (2012). “Surface Quasigeostrophic Solutions and Baroclinic Modes with Exponential Stratification”. In: *Journal of Physical Oceanography* 42.4, pp. 569 –580. DOI: [10.1175/JPO-D-11-0111.1](https://doi.org/10.1175/JPO-D-11-0111.1) (cit. on p. 26).
- LaCasce, J. H. and Sjoerd Groeskamp (2020). “Baroclinic Modes over Rough Bathymetry and the Surface Deformation Radius”. In: *Journal of Physical Oceanography* 50.10, pp. 2835 –2847. DOI: [10.1175/JPO-D-20-0055.1](https://doi.org/10.1175/JPO-D-20-0055.1) (cit. on pp. 27, 37).
- Le Traon, Pierre Yves et al. (2019). “From Observation to Information and Users: The Copernicus Marine Service Perspective”. In: *Frontiers in Marine Science*. DOI: [10.3389/fmars.2019.00234](https://doi.org/10.3389/fmars.2019.00234) (cit. on p. 39).
- Liu, Guangpeng, Annalisa Bracco, and Alexandra Sitar (2021). “Submesoscale Mixing Across the Mixed Layer in the Gulf of Mexico”. In: *Frontiers in Marine Science* 8. ISSN: 2296-7745. DOI: [10.3389/fmars.2021.615066](https://doi.org/10.3389/fmars.2021.615066) (cit. on p. 24).
- McWilliams, James C. (2016). “Submesoscale currents in the ocean”. In: *Proc. R. Soc. A* 472:20160117. DOI: [10.1098/rspa.2016.0117](https://doi.org/10.1098/rspa.2016.0117) (cit. on pp. 15–18, 20).
- Mensa, Jean Alberto, Zulema Garraffo, Annalisa Griffa, Tamay Mehmet Ozgokmen, Angelique Haza, and Veneziani Milena (2013). “Seasonality of the submesoscale dynamics in the Gulf Stream region”. In: *Ocean Dynamics*. ISSN: 1616-7228. DOI: [10.1007/s10236-013-0633-1](https://doi.org/10.1007/s10236-013-0633-1) (cit. on pp. 21, 38).
- Numerov, B. V. (1927). “Note on the numerical integration of  $d^2x/dt^2 = f(x, t)$ ”. In: *Astronomische Nachrichten* 230.19, pp. 359–364. DOI: [10.1002/asna.19272301903](https://doi.org/10.1002/asna.19272301903) (cit. on p. 28).

- Numerov, B.V. (June 1924). “A Method of Extrapolation of Perturbations”. In: *Monthly Notices of the Royal Astronomical Society* 84.8, pp. 592–602. ISSN: 0035-8711. DOI: [10.1093/mnras/84.8.592](https://doi.org/10.1093/mnras/84.8.592) (cit. on p. 28).
- Pedlosky, Joseph (1987). *Geophysical fluid dynamics*. Ed. by New York Springer-Verlag. 2nd edition (cit. on pp. 24, 26).
- Pettenuzzo, D., W. G. Large, and N. Pinardi (2010). “On the corrections of ERA-40 surface flux products consistent with the Mediterranean heat and water budgets and the connection between basin surface total heat flux and NAO”. In: *J. Geophys. Res.* 115, C06022. DOI: [10.1029/2009JC005631](https://doi.org/10.1029/2009JC005631) (cit. on p. 39).
- Pinardi, N., I. Allen, E. Demirov, P. De Mey, G. Korres, A. Lascaratos, P.Y. Le Traon, et al. (2003). “The Mediterranean ocean forecasting system: first phase of implementation (1998-2001)”. In: *Annales Geophysicae*. DOI: [10.5194/angeo-21-3-2003](https://doi.org/10.5194/angeo-21-3-2003) (cit. on p. 36).
- Rocha, C., S. Gille, T. Chereskin, and D. Menemenlis (2016). “Seasonality of submesoscale dynamics in the Kuroshio Extension”. In: *Geophysical Research Letters*, 43(21), 11304-11311. DOI: [10.1002/2016GL071349](https://doi.org/10.1002/2016GL071349) (cit. on p. 22).
- Sasaki, Hideharu, Bo Qiu, Patrice Klein, Yoshikazu Sasai, and Masami Nonaka (2020). “Interannual to Decadal Variations of Submesoscale Motions around the North Pacific Subtropical Countercurrent”. In: *Fluids* 5.3. ISSN: 2311-5521. DOI: [10.3390/fluids5030116](https://doi.org/10.3390/fluids5030116) (cit. on p. 22).
- Simoncelli, Simona, Nadia Pinardi, Paolo Oddo, Arthur J. Mariano, Giuseppe Montanari, Attilio Rinaldi, and Marco Deserti (2011). “Coastal Rapid Environmental Assessment in the Northern Adriatic Sea”. In: *Dynamics of Atmospheres and Oceans* 52.1. Special issue of Dynamics of Atmospheres and Oceans in honor of Prof. A.R. Robinson, pp. 250–283. ISSN: 0377-0265. DOI: [10.1016/j.dynatmoce.2011.04.004](https://doi.org/10.1016/j.dynatmoce.2011.04.004) (cit. on p. 38).
- Talley, Lynne D., George L. Pickard, William J. Emery, and James H. Swift (2011). “Chapter 1 - Introduction to Descriptive Physical Oceanography; Chapter 9 - Atlantic Ocean; Chapter 14 - Global Circulation and Water Properties”. In: *Descriptive Physical Oceanography (Sixth Edition)*. Ed. by Lynne D. Talley, George L. Pickard, William J. Emery, and James H. Swift. Sixth Edition. Boston: Academic Press, pp. 245–301. ISBN: 978-0-7506-4552-2. DOI: [10.1016/B978-0-7506-4552-2.10009-5](https://doi.org/10.1016/B978-0-7506-4552-2.10009-5) (cit. on pp. 13, 36–38).

- Trotta, Francesco, Elisa Fenua, Nadia Pinardi, Diego Bruciaferri, Luca Giacomelli, Ivan Federico, and Giovanni Coppini (2016). “A Structured and Unstructured grid Relocatable ocean platform for Forecasting (SURF)”. In: *Deep Sea Research Part II: Topical Studies in Oceanography* 133. Physical, chemical and biological observations and modelling of oil spills in the Mediterranean Sea, pp. 54–75. ISSN: 0967-0645. DOI: [10.1016/j.dsr2.2016.05.004](https://doi.org/10.1016/j.dsr2.2016.05.004) (cit. on pp. 21, 34).
- Trotta, Francesco, Nadia Pinardi, Ivan Federico, Giovanni Coppini, Causio S., Jansen E., Iovino D., and Masina S. (2021). “A Relocatable Ocean Modeling Platform for Downscaling to Shelf-Coastal Areas to Support Disaster Risk Reduction”. In: *Front. Mar. Sci.* 8:642815. DOI: [10.3389/fmars.2021.642815](https://doi.org/10.3389/fmars.2021.642815) (cit. on pp. 21, 34).
- Trotta, Francesco, Nadia Pinardi, Elisa Fenu, Alessandro Grandi, and Vladyslav Lyubartsev (2017). “Multi-nest high-resolution model of submesoscale circulation features in the Gulf of Taranto”. In: *Ocean Dynamics* 67, 1609–1625. DOI: [10.1007/s10236-017-1110-z](https://doi.org/10.1007/s10236-017-1110-z) (cit. on p. 21).
- Uchida, T. et al. (2022). “Cloud-based framework for inter-comparing submesoscale-permitting realistic ocean models”. In: *Geoscientific Model Development* 15.14, pp. 5829–5856. DOI: [10.5194/gmd-15-5829-2022](https://doi.org/10.5194/gmd-15-5829-2022) (cit. on p. 21).
- Wessel, Paul and Walter Smith (Apr. 1996). “A global, self-consistent, hierarchical, high-resolution shoreline database”. In: *Journal of Geophysical Research* 101, pp. 8741–8743. DOI: [10.1029/96JB00104](https://doi.org/10.1029/96JB00104) (cit. on p. 41).
- Zhang, Xu, JING Zhiyou, ZHENG Ruixi, HUANG Xiaolong, and CAO Haijin (2021). “Submesoscale characteristics of a typical anticyclonic mesoscale eddy in Kuroshio Extension”. In: *Journal of Tropical Oceanography*, 40(6) 31–40. DOI: [10.11978/2020152](https://doi.org/10.11978/2020152) (cit. on p. 22).

